

**HIGH TEMPERATURE LEAKAGE PERFORMANCE OF A
HYBRID BRUSH SEAL COMPARED TO A STANDARD BRUSH
SEAL AND A LABYRINTH SEAL**

A Thesis

by

ZACHARY SPENCER ASHTON

Submitted to the Office of Graduate Studies of
Texas A&M University
in partial fulfillment of the requirements for the degree of
MASTER OF SCIENCE

August 2009

Major Subject: Mechanical Engineering

**HIGH TEMPERATURE LEAKAGE PERFORMANCE OF A
HYBRID BRUSH SEAL COMPARED TO A STANDARD BRUSH
SEAL AND A LABYRINTH SEAL**

A Thesis

by

ZACHARY SPENCER ASHTON

Submitted to the Office of Graduate Studies of
Texas A&M University
in partial fulfillment of the requirements for the degree of
MASTER OF SCIENCE

Approved by:

Chair of Committee, Luis San Andrés
Committee Members, Alan Palazzolo
Peter Keating
Head of Department, Dennis L. O'Neal

August 2009

Major Subject: Mechanical Engineering

ABSTRACT

High Temperature Leakage Performance of a Hybrid Brush Seal Compared to a Standard Brush Seal and a Labyrinth Seal. (August 2009)

Zachary Spencer Ashton, B.S., Clemson University

Chair of Advisory Committee: Dr. Luis San Andrés

Adequate sealing in turbomachinery reduces secondary leakage and results in more efficient and stable systems. Labyrinth seals are most common, although brush seals are popular in specialized applications. The Hybrid Brush Seal (HBS) is a novel design that adds to the bristle brush matrix a number of cantilever pads that rest on the rotor surface. Upon shaft rotation the pads lift due to the generation of a hydrodynamic gas film while the brushes effectively seal an upstream pressure. Hence the HBS has no wear and no local thermal distortion effects.

Measurements of leakage versus pressure differential are obtained in a three-teeth labyrinth, a conventional brush seal, and a hybrid brush seal for operation at high temperature (300°C), with shaft surface speeds to 27 m/s, and at supply pressures to 3.5 bar. Flow measurements are presented in terms of a flow factor to remove dependency on the air temperature and supply pressure. The measurements demonstrate the HBS leaks less (~61%) than a standard brush seal and is significantly better (~38%) than a similarly sized labyrinth seal. Predictions of flow through a labyrinth seal predict well at supply pressures under 1.7 bar but overpredict by as much as 25% at high supply pressures. A porous medium fluid flow model predicts the flow through the HBS and brush seal. The model for the HBS and brush seal underpredicts the flow rate at low supply pressures but match well at high supply pressures.

Measurements of the drag torque of the test seals show the HBS has a larger torque when pressurized compared to the brush seal and labyrinth seal. This indicates that the HBS experiences a larger degree of blow-down due to the pads decreasing the clearance.

The mechanical parameters of the brush seal and HBS are found based upon the flexibility function from impact load tests. A combined structural and dry friction damping model represent well the measured flexibility. An equivalent damping is found based upon the energy dissipation. Based upon the damping ratio, the HBS has twice of the viscous damping as the brush seal at a supply pressure of 2.0 bar.

DEDICATION

To my wife, Anna, for her covenantal love and support through all times. I am so blessed to have you by my side. To my son, Owen, for the joy he has brought to our lives. To my parents, Mark and Cathy, for their continual love and guidance.

ACKNOWLEDGEMENTS

Thanks to Dr. Luis San Andrés, my advisor and committee chair, for providing the opportunity to research the problem presented. His technical guidance and support have been invaluable for the duration of this research.

Thanks to Dr. Adolfo Delgado for educating me in the details of the test rig and of the previously work done on Hybrid Brush Seals. His experience at the Texas A&M University Turbomachinery Laboratory provided a strong foundation upon which to build the body of research. Additionally, thanks to the other students at the Turbomachinery Lab who have provided help along the way.

Thanks to Brian Butler for the excellent work in the construction of a wide range of components for the test rig. His knowledge and expertise have been essential in the creation of the high temperature rig.

Thanks to the sponsor, Siemens Power Generation, for providing financial support for the duration of the project and to John Justak of Advanced Technology Group, Inc. for providing the test brush seal and HBS.

NOMENCLATURE

A	πDC_r . Flow area in non-contacting clearance seal [m ²]
C_{eq}	System equivalent damping [N-s/m]
C_r	$ID_s - OD_d$. Seal radial Clearance [m]
D	OD_d . Rotor diameter [m]
F	Input force to system [N]
I	Shaft and disc area moment of inertia [m ⁴]
ID_h	Air cylinder housing inner diameter [m]
ID_s	Seal ring inner diameter [m]
IF	Interference fit between housing and seal [m]
$k_{V\omega}$	V/ω . Motor constant [V.sec/rad]
K_{eq}	System equivalent stiffness [N/m]
l	Seal axial length [m]
L	Shaft length [m]
L_e	Location of displacement measurements and impact load [m]
L_s	Location of test seal [m]
\dot{m}	Mass flow rate [kg/s]
M_d	Mass of disc [kg]
M_{eq}	System equivalent mass [kg]
N_T	Number of teeth in labyrinth seal
OD_s	Seal ring outer diameter [m]
OD_d	Disc outer diameter [m]
P	Gas (absolute) pressure in seal [Pa]
P_e	Absolute exhaust pressure [Pa]
P_s	Absolute supply pressure [Pa]
P_r	Pressure ratio (P_s/P_e)
\wp	$(V \times i)$. Motor power (voltage x current) [W]

\mathfrak{R}_g	Gas constant [J/kg-K]
X	Displacement response of disc at sensor location [m]
T	Gas temperature [K]
T_{orque}	$\frac{\phi}{\omega}$. Motor Torque [N.m]
α_b	Bristle material thermal expansion coefficient [$13.5 \cdot 10^{-6} / ^\circ\text{C}$]
α_d	Disc material thermal expansion coefficient [$11.2 \cdot 10^{-6} / ^\circ\text{C}$]
α_h	Cylinder housing material thermal expansion coefficient [$12 \cdot 10^{-6} / ^\circ\text{C}$]
α_s	Seal ring material thermal expansion coefficient
	Labyrinth seal: [$23.6 \cdot 10^{-6} / ^\circ\text{C}$]
	Brush seal and HBS: [$12 \cdot 10^{-6} / ^\circ\text{C}$]
ρ	Shaft and disc density [kg / m^3]
γ_{eq}	Equivalent structural damping
μ	Dry friction damping
μ_i	Flow coefficient
μ_0	Kinetic-energy carryover factor
θ	Bristle lay angle [degrees]
Φ	$\left(\frac{\dot{m}\sqrt{T}}{P_s D} \right)$ Flow factor [$\text{kg} \cdot \text{K}^{0.5} / (\text{MPa} \cdot \text{m} \cdot \text{s})$]
ψ	Shape function for cantilevered beam
Φ_M	$\left(\frac{\dot{m}l\sqrt{T}}{P_s D} \right)$ Modified flow factor [$\text{kg} \cdot \text{K}^{0.5} / (\text{MPa} \cdot \text{s})$]
ω	Shaft angular speed [rad/s]
ω_n	System natural frequency [rad/s]
ζ	$\left(\frac{C_{eq}}{2\sqrt{K_{eq}M_{eq}}} \right)$ Viscous damping ratio

TABLE OF CONTENTS

	Page
ABSTRACT	iii
DEDICATION.....	v
ACKNOWLEDGEMENTS	vi
NOMENCLATURE	vii
TABLE OF CONTENTS.....	ix
LIST OF FIGURES	xii
LIST OF TABLES.....	xvi
 CHAPTER	
I INTRODUCTION.....	1
II LITERATURE REVIEW	4
Seals for Gas Turbines	4
Labyrinth Seals	5
Brush Seals	7
Hybrid Brush Seals	9
III HIGH TEMPERATURE TEST APPARATUS	12
Seal Test Rig.....	12
Test Seals.....	17
IV LEAKAGE MEASUREMENT IN A THREE-TEETH LABYRINTH	
SEAL.....	20
Experimental Procedure	20
Results and Discussion.....	21

CHAPTER	Page
V	MEASUREMENTS OF CLEARANCE AND LEAKAGE PREDICTIONS FOR A TEST THREE-TEETH LABYRINTH
	SEAL..... 25
	Experimental Procedure 25
	Results and Discussion..... 27
VI	LEAKAGE MEASUREMENT IN A CONVENTIONAL BRUSH
	SEAL..... 36
	Experimental Procedure 36
	Results and Discussion..... 37
VII	LEAKAGE MEASUREMENTS IN A HYBRID BRUSH SEAL 41
	Experimental Procedure 41
	Results and Discussion..... 41
VIII	COMPARISON OF LEAKAGE FOR THREE TEST SEALS 46
IX	SEALS DRAG TORQUE AT AMBIENT TEMPERATURE 50
	Experimental Procedure 50
	Results and Discussion..... 51
X	IDENTIFICATION OF SEAL EQUIVALENT MECHANICAL PARAMETERS FROM IMPACT LOAD TESTS 55
	Experimental Procedure 55
	Results and Discussion..... 59
XI	CONCLUSIONS AND RECOMMENDATIONS..... 64
	REFERENCES 67

	Page
APPENDIX A: CALIBRATION OF FLOW METER FOR OPERATION AT A RANGE OF PRESSURES AND TEMPERATURES.....	70
APPENDIX B: CALIBRATION OF PRESSURE SENSOR.....	72
APPENDIX C: USER INTERFACE FOR DATA ACQUISITION AND CONTROL	74
APPENDIX D: CALIBRATION OF HIGH TEMPERATURE OPTICAL SENSORS	76
APPENDIX E: ROTOR WEAR DUE TO SEAL CONTACT	77
VITA.....	79

LIST OF FIGURES

	Page
Figure 1: View of downstream (left) and inside view of teeth (right) of a three-teeth labyrinth seal.	5
Figure 2: Upstream (left) and downstream (right) view of a conventional brush seal with brushes on the upstream and the backing plate on the downstream side.....	7
Figure 3: Upstream (left) and downstream (right) view of a HBS with brushes on the upstream and the cantilever pads on the downstream side.....	10
Figure 4: High temperature seal test rig with major components.....	12
Figure 5: Cutaway view of the pressurization cylinder with instrumentation.	14
Figure 6: Cutaway view of the shaft support with tapered roller bearings.	15
Figure 7: Cutaway view on disc centering system with fiber optic displacement sensors.....	16
Figure 8: Soft mounted shaker connecting to shaft via load cell and stinger.....	17
Figure 9: Dimensions of three-teeth labyrinth seal for leakage measurements.....	20
Figure 10: Mass flow rate for three-teeth labyrinth versus pressure ratio for various inlet gas temperatures (30-300°C). Rotor speed at 3,000 RPM.	22
Figure 11: Flow factor Φ for three-teeth labyrinth seal versus pressure ratio (supply/exhaust) for varying inlet temperatures (30-300°C). Rotor speed at 3,000 RPM.	23
Figure 12: Mass flow rate for three-teeth labyrinth seal versus rotor speed at three pressure ratios ($PR=P_s/P_e=1.2,2.0,2.8$). Air inlet temperature of 300°C.....	24
Figure 13: Seal centering device and optical sensors for measuring gap in horizontal and vertical directions.	26
Figure 14: Location of thermocouples viewed from the downstream end (low pressure side) with exhaust duct removed. Thermocouple on housing is located on the outer surface of housing (exposed to ambient air).....	27

Figure 15: Temporal evolution of temperatures at various locations in test rig for three-teeth labyrinth seal. Constant air flow at 35 g/s. Air inlet temperature vs. time specified.....	28
Figure 16: Temporal evolution of diametral clearance and air inlet temperature (nominal clearance of 1.04 mm at room temperature) in three-teeth labyrinth seal. Operation with constant flow at 35 g/s. No shaft rotation. ...	29
Figure 17: Temporal evolution of supply pressure and air inlet temperature and in three-teeth labyrinth seal. Operation with constant flow at 35 g/s.....	29
Figure 18: Three-teeth labyrinth seal diametral clearance using feeler gauges and predictions versus gas inlet temperature. No shaft rotation.	31
Figure 19: Predicted mass flow rate versus (inlet/exhaust) pressure ratio for three-teeth labyrinth seal using model and XLLaby©. No shaft rotation. Predictions based on measured clearance at 30°C and 300°C (0.52 mm).	33
Figure 20: Predicted and measured mass flow rate versus (inlet/exhaust) pressure ratio for three-teeth labyrinth seal at two inlet temperatures. No shaft rotation. Predictions based on two distinct (measured) clearances.	34
Figure 21: Predicted and experimental flow factor Φ versus (inlet/exhaust) pressure ratio for three-teeth labyrinth seal at two inlet temperatures. No shaft rotation. Predictions based on two distinct clearances.	35
Figure 22: Mass flow rate for conventional brush seal versus pressure ratio (supply/exhaust) for varying inlet temperatures (30-300°C). Rotor Speed at 3,000 RPM.	37
Figure 23: Flow factor Φ for conventional brush seal versus pressure ratio (supply/exhaust) for varying inlet temperatures (30-300°C). Rotor speed of 3,000 RPM.	38
Figure 24: Mass flow rate for conventional brush seal versus rotor speed at three pressure ratios ($PR=P_s/P_e=1.3,1.7,3.0$). Air inlet temperature of 300°C.....	39

Figure 25: Comparison of predicted and measured mass flow rates in brush seal versus pressure ratio $[P_s/P_e]$. Rotor speed of 3000 RPM. Air inlet temperature at 300°C. Predictions from model in [25].....	40
Figure 26: Mass flow rate for HBS versus pressure ratio (supply/exhaust) for varying inlet temperatures (30-300°C). Rotor speed at 3,000 RPM.....	42
Figure 27: Flow factor Φ for HBS versus pressure ratio (supply/exhaust) for varying inlet temperatures (30-300°C). Rotor speed of 3,000 RPM.	43
Figure 28: Mass flow rate for HBS versus rotor speed at three pressure ratios ($PR=P_s/P_e=1.5,2.5,3.6$). Air inlet temperature of 300°C	44
Figure 29: Comparison of predicted and measured mass flow rate in HBS versus pressure ratio $[P_s/P_e]$. Rotor speed of 1000 RPM. Air inlet temperature at 300°C.....	45
Figure 30: Flow factor Φ for three test seals versus pressure ratio $[P_s/P_e]$. Air inlet temperature at 300°C. Rotor speed at 3,000 RPM.	46
Figure 31: Modified flow factor Φ_M for three seal types versus pressure ratio $[P_s/P_e]$. Air inlet temperature at 300°C. Rotor speed at 3,000 RPM.	48
Figure 32: Mass flow rate versus pressure ratio $[P_s/P_e]$ for current HBS and previous HBS (Ref [22]). Air inlet temperature at 30°C. Rotor speed at 1,000 RPM and 600 RPM for the current HBS and previous HBS, respectively.	49
Figure 33: Baseline motor power versus rotor speed. No gas pressurization.	51
Figure 34: Baseline motor voltage and drag torque versus rotor speed. No gas pressurization. Ambient temperature. Motor speed constant $k_{V\omega}=V/\omega = 0.24$ V-s/rad (0.025 V/rpm).	52
Figure 35: Motor torque versus rotor speed for three seals with supply pressure of 2 bar. Tests without pressures (no leakage) also shown. Operation at ambient temperature (25°C).	53

Figure 36: Torque versus rotor speed for current HBS and other HBS operating at inlet pressure up to 2.0 bar and 1.7 bar, respectively. Operation at ambient temperature (25°C).	54
Figure 37: First mode shape of test rotor and element model with structural and support elements.....	56
Figure 38: Schematic view of shaft-disc and seal assembly and its equivalent representation as a single degree of freedom mechanical system.....	57
Figure 39: Amplitude of flexibility function for test rotor and hybrid brush seal (HBS). Tests with air at supply pressure/exhaust pressure (PR)=1.5 and 2.0. Baseline (no seal) and with seal and no pressurization (PR=1.0) included. Impact load tests. No shaft rotation. Ambient temperature=25°C.....	59
Figure 40: Amplitude of flexibility function for test rotor and brush seal. Tests with air at supply pressure/exhaust pressure (PR)=1.5 and 2.0. Baseline (no seal) and with seal and no pressurization (PR=1.0) included. Impact load tests. No shaft rotation. Ambient temperature=25°C	60
Figure 41: Measured flexibility in HBS and physical models with (a) structural damping-dry friction and (b) viscous damping. Supply pressure ~ 2.0 bar. Ambient temperature, no shaft rotation.	62
Figure 42: Measured flexibility in brush seal and physical models with (a) structural damping-dry friction and (b) viscous damping. Supply pressure ~ 2.0 bar. Ambient temperature, no shaft rotation.	62
Figure 43: Measured flexibility of test system without a seal in place and physical models with (a) structural damping-dry friction and (b) viscous damping. Ambient temperature, no shaft rotation, no pressurization.....	63

LIST OF TABLES

	Page
Table 1: Test seals-geometry and material properties	19
Table 2: Pressurized cylinder air temperature and shaft speed for labyrinth seal leakage tests	21
Table 3: Uncertainty for pressure ratio and mass flow rate in labyrinth seal.....	22
Table 4: Uncertainty for pressure ratio and mass flow rate in conventional brush seal.....	38
Table 5: Uncertainty for pressure ratio and mass flow rate in conventional brush seal.....	42
Table 6: Equivalent system coefficients with HBS and brush seal at three supply pressures. Air inlet at 25°C. No shaft rotation.	61

CHAPTER I

INTRODUCTION

Seals in turbomachinery affect both the efficiency, through leakage control, and the rotordynamic stability of the entire system [1]. Improving seal design is often the most cost-effective way to increase performance by limiting secondary leakage [1]. As efficiency and power output requirements for turbomachinery rise, higher temperatures, pressures, and shaft speeds become prevalent. Seals must be able to restrict flow while withstanding often inclement conditions.

Labyrinth seals are non-contacting elements that provide an inexpensive and simple method of obstructing flow from a high pressure region to a low pressure region [2]. The design of the labyrinth seal is fairly simple and can be made to accommodate a large range of sizes and operating conditions. New developments in labyrinth seals have increased efficiency and decreased the likelihood of unstable rotor-bearing system operation. The labyrinth seal, however, still allows a relatively large amount of leakage because of its inherent clearance between the seal and rotor. A clearance must always be present during long-term labyrinth seal operation. Clearances are enlarged due to intermittent contact and wear at start-up and shutdown. The design of the labyrinth seals in high temperature environments must include considerations for the thermal expansion of the seal and rotor as well as considerations for windage heating. In certain instances, long labyrinth seals may lead to rotordynamic instability due to swirling shear induced flow in the circumferential direction [1].

In some industrial applications [3], brush seals replace labyrinth seals at the locations of secondary leakage. The brush seal can exhibit leakage as low as 10% that of a similarly sized labyrinth seal and will not excite a rotordynamic instability [3]. The decrease in leakage renders higher engine efficiency in two ways. The brush seal allows

This thesis follows the style of the ASME Journal of Tribology.

less pressurized gas to escape and permits the rotor length and weight to decrease. In addition to the benefit of less leakage, the brush seal can handle rotor radial movement due to the soft structural stiffness of its bristles. The bristles are known to blow-down during operation. Blow-down is described as the bristles moving radially towards the rotor. This effect can aid to further decrease leakage. However, the brush seal best limits leakage when in contact with its rotating disc. Contact leads to an increase in drag torque and localized heat generation. Most brush seals are designed to rub until the proper level of interference is reached. Therefore, certain design tradeoffs exist to minimize leakage while preventing thermal instability of a brush seal due to excessive contact [4]. The brush seal also only allows rotation in one direction due to the lay angle of the bristles. Any degree of rotation in the opposing direction will often cause the bristles to buckle and deform. Further, brush seals suffer from poor axial stiffness as the bristles tend to bend in the direction of the pressure drop. This axial bending is controlled by the length the bristles extend past the backing support plate. If the bristles are too long, and the bending is excessive; the bristle tips may disconnect from the disc and allow a large amount of leakage.

The Hybrid Brush Seal (HBS) seeks to improve engine performance and reliability in comparison to labyrinth seals and brush seals. The HBS incorporates to the bristle matrix of a brush seal a number of cantilever pads that initially rest on the rotor surface when the rotor is not spinning [5]. HBSs have shown potential to decrease secondary leakage by greater amounts than a shoed brush seals [6]. The design permits radial movement of the rotor similar to a brush seal but with the added benefit of a high degree of seal axial stiffness. This increase in axial stiffness should allow the HBS to operate at higher pressure differentials. The HBS is designed to limited heat generation since the pads experience a hydrodynamic lift from a thin air film during operation [5]. Further, the HBS allows the benefit of rotor rotation in both directions. Due to the initial contact, however, the HBS has high levels of drag torque during unpressurized conditions such as those experienced during machine start-up [6].

For this novel technology to continue its advancement, its leakage, drag torque, wear rate, and vibration characteristics must be quantified for a range of operating temperatures, pressure differentials, and rotational speeds. The performance of the HBS can then be directly compared to the performance of labyrinth seals and brush seals at similar conditions. Direct comparisons of performance may provide the necessary motivation for OEMs to consider updating existing seals. Furthermore, when introducing a new component into a rotating machine, it is critical to quantify its impact on the behavior and life of the overall system.

CHAPTER II

LITERATURE REVIEW

Seals for Gas Turbines

This literature review discusses the general requirements for secondary seals in turbomachinery. The review also reports on the previous research, detailing the advantages and disadvantages, of two well established seals: labyrinth and brush. Additionally, discussion is given to previous research on the Hybrid Brush Seal (HBS) and its demonstrated potential to provide effective sealing at ambient temperature conditions with reduced wear and increased radial stiffness. The previous research serves as the basis for the high temperature measurements and predictions which follow the literature review.

Chupp et al. [1] provide a comprehensive review of the uses and benefits of sealing in turbomachinery. The review also discusses the location for seals and the benefits and disadvantages for specific sealing methods. The seal types reviewed are for use in both aero and land based gas turbines. During typical operation, interstage turbine seals may experience temperatures up to 600°C and absolute pressure differentials of 2.1 MPa [1]. Under these conditions growth of components and wear become increasingly important to the life and performance of the seals. Over time, wear can drastically affect the effectiveness of the seal and the overall efficiency of the turbomachine.

Floyd [2] discusses three main categories for rotary seals: clearance seals, contact seals, and gas film seals. Contact and gas film seals provide the best leakage resistance but are limited by the pressure differentials and surface speeds. As the pressure differential and speed increase for contact seals, the rotating and stationary surfaces begin to experience high levels of heating due to dry friction. This heating can lead to thermal instabilities that could lead to high leakages at best, or complete machine failure at worst. Therefore, careful design plays a critical role in all sealing methods, but particularly in those which can come in contact with the rotating component. New

materials, coatings in particular, and novel designs for contact seals continue to expand the boundary for acceptable operating conditions.

Labyrinth Seals

Labyrinth seals represent the most prevalent means of reducing secondary leakage. Labyrinth seals are clearance annular seals that operate with a gap between the stationary and rotating component [1]. Figure 1 presents a basic three-teeth labyrinth seal. The basic design of a labyrinth seal consists of a ring with multiple thin teeth spaced axially running along the circumference of the seal ring [2]. The effectiveness of a labyrinth seal is largely determined by the actual clearance between the tips of the teeth and the opposing surface. Floyd [2] states that labyrinth seals typically have a radial clearance (C) of 0.25-0.5 mm, while Childs [7] discusses cases with radial clearance to radius ratios (C/R) of 0.0016-0.0076.

Demands for better performance led to design modifications such as steps, honeycomb lands, and abradable contact surfaces [1]. The improvements allow for the teeth to operate at a lower clearance with better wear characteristics in the case of radial contact. The wear will eventually rub away the inner diameter of the seal until a sufficient clearance develops. All of these designs, however, work on the basic principle that a high pressure gas flow is retarded by the presence of a sharp-edged obstruction which leads to a lower pressure in the succeeding cavity. Additional labyrinths can be placed in parallel to add flow resistance thus decreasing further the leakage.

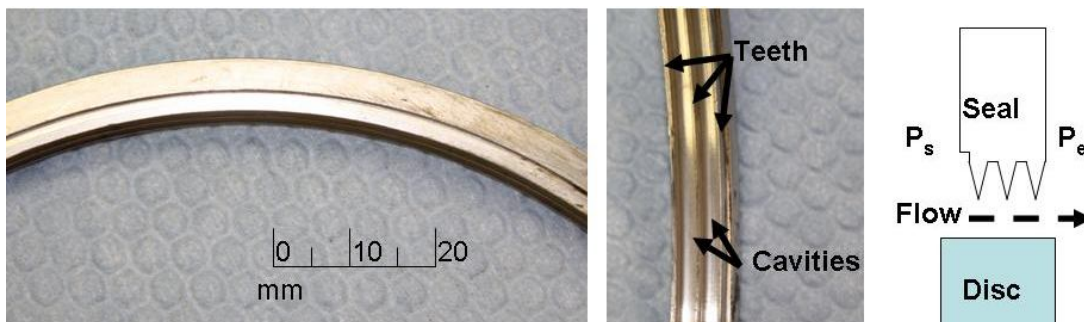


Figure 1: View of downstream (left) and inside view of teeth (right) of a three-teeth labyrinth seal.

Due to the simplicity of this design, labyrinth seals cost less to manufacture than many other options and can be used over a wide range of operating temperatures, rotor speeds, and pressures. Labyrinth seals can also be manufactured as rings or segmented for easy installation, particularly for large land-based gas turbines. Floyd [1] states that there are no limitations to the surface speed and pressure differential in which non-contacting seals, such as the labyrinth seal, can withstand. El-Gamal et al. [8] demonstrate theoretically that shaft speed has no effect on the leakage performance of typical straight through labyrinth seals.

Design of labyrinth seals operating at high temperatures requires considerations for the thermal growth of the seal and the rotor so that an allowable clearance is maintained during normal operation. The radial clearance must also be large enough to permit the radial excursions of the rotor for the particular operation and running speed at which it is being used. The flow through the clearance can also introduce cross-coupled stiffness due to circumferential swirl in the cavity, which may lead to rotor-bearing instability [9]. Childs et al. [10] effectively use swirl brakes to lower cross-coupled stiffnesses that lead to rotordynamic instability.

Denecke et al. [11] show that a complex relationship exists between the heating of the air traveling through a labyrinth seal and the development of circumferential swirl. Choi et al. [12] show that small clearances and a large tooth pitch can reduce the seal leakage. However, small clearances also lead to more windage heating and shorter part life. The heating can lead to changes in clearance, higher operating torques, and even shaft bowing. Further, hot air ingestion may prove harmful to the succeeding turbine stages. Therefore, it is particularly important to understand the heating and rotordynamic effects in axially long labyrinth seals, since these seals typically are most prone to develop undesirable circumferential swirl flow.

Effective labyrinth seal designs often require multiple seals working in parallel to step down from the supply pressure to the discharge pressure. This can result in multiple sections of labyrinth seals over the course of a lengthy axial segment. As the axial

length of the shaft is increased, the shaft becomes heavier and the engine has a lower efficiency. Additionally, the natural frequency of the system will decrease with a longer rotor.

Brush Seals

Brush seals may increase engine efficiency by up to one-sixth ($1/6$) of a percentage point [4]. The brush seal design consists of a bed of densely packed metallic or plastic bristles attached to an outer ring. Figure 2 displays a typical brush seal from upstream and downstream views. Common practice requires that the bristle tips contact the rotating shaft during operation. If the bristles lose contact, performance will drastically decrease. On the exhaust side of the seal, a back plate prevents the bristles from extreme axial bending caused by the imposed pressure differential [3]. The bristles are set at a specific lay angle, usually between 30° and 60° , in the direction of shaft rotation. The rotor must rotate in the direction of the bristle lay angle; otherwise, the bristles will buckle and distort causing higher levels of leakage [1].

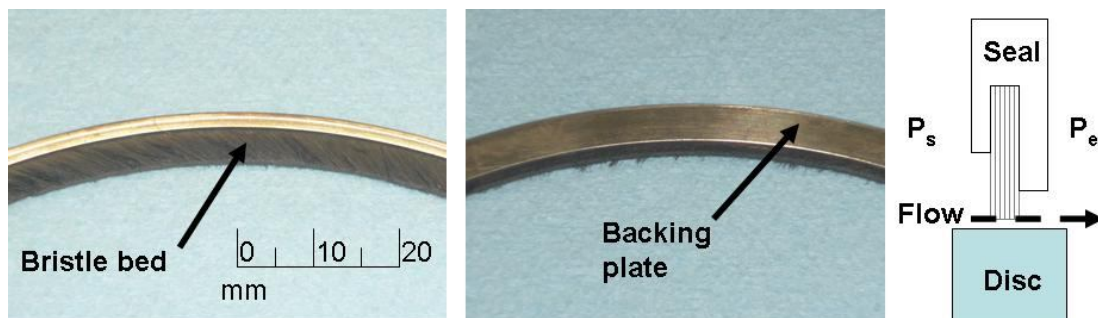


Figure 2: Upstream (left) and downstream (right) view of a conventional brush seal with brushes on the upstream and the backing plate on the downstream side.

Ferguson reports the brush seals can result in as low as 10% of the leakage of a similarly sized labyrinth seal [3]. Since the brush seal exhibits a lower leakage per axial length, the rotor length and weight decrease. Ferguson [3] first discusses the phenomenon of brush seal blow-down and the benefit on leakage performance. Blow-down is described as the bristles of the seal moving in towards the rotor during

pressurized operation. This action serves to reduce leakage while increasing the drag torque. Two main forces drive the phenomenon: axial compression of the bristle pack and aerodynamic forces on the bristle tips. Crudginton and Bowher [13] discuss axial compression due to the pressure differential as the source of blow down. The authors [13] compare the level of blow-down using measurements of bristle movement and Finite Element Analysis (FEA) model results and find that torque increases nearly linearly as a function of interference and pressure drop. They also determine the magnitude of clearance to estimate the blow-down for different pressure differences. Crudginton and Bowher [13] find that the blow-down can be broken into two types of regimes with respect to the pressure drop: a linear increase up to a pressure drop of 1 bar, followed by a constant level of blow-down for pressure differentials above 1 bar. Franceschini et al. [14] study blow down due to aerodynamic forces on the bristles. These forces create a moment on the bristle tip, pulling the bristles closer to the rotor. As with the axial compression of the bristle pack, the aerodynamic forces increase at higher pressure differentials.

Brush seals are known to not promote rotordynamic instability. Conner and Childs [15] present rotordynamic measurements of a four-stage brush seal. Their results show low and often times stabilizing cross-coupled stiffnesses. Chupp et al. [1] also note that, because of their inherent compliance, brush seals are better suited to handle rotor excursion during transient excursions. However, brush seal stiffening or bristle hysteresis can sometimes occur due to excursions of the rotor into the bristles. Basu et al. [16] describe the phenomenon in which the bristles fail to close onto the rotor after some excursion, thus resulting in a significantly higher leakage and decreasing the efficiency of the machine. Zhao and Stango [17] study the interbristle forces causing brush seal hysteresis; finding that brush seals with the smallest lay angles are least likely to experience hysteresis.

Brush seal design is critical to proper operation. Dinc et al. [18] outline the general process to designing brush seals. Bristle length is one of the greatest design tradeoffs. Short bristle packs can cause failure if radial excursions of the shaft cause contact with

the back plate. If the bristles are too long, on the other hand, the pressure differential causes the bristles to buckle thus reducing the effectiveness of the seal to prevent leakage [4]. Additionally, design considerations are involved with the level of contact the bristles make with the rotating component. If the contact is too hard, the rub may cause excessive frictional heating which causes thermal growth in the interference. This leads to more friction and rotor growth until the seal fails. This represents a thermal instability. Too little interference, however, may result in a higher mass flow rate, negating the seal usefulness.

Proper brush seal operation also requires considerations for multiple frictional interactions within the seal itself. Aksit [19] shows analysis of the stresses due to the frictional interactions of brush seals. These interactions can be classed into three categories: interbristle contact, bristle to back plate contact, and bristle to rotor contact. Each of these factors can limit the life of the brush seal leading to unscheduled engine maintenance, and even possible overhaul for seal replacement. Further, the friction in brush seals may lead to high levels of drag torque during shaft rotation. Friction between the bristles is also likely to cause high levels of hysteresis in brush seals.

Hybrid Brush Seals

The HBS is a novel design developed to further limit secondary leakage. Justak [5] claims leakage equivalent to a similarly sized labyrinth seal at 0.038 mm radial clearance. As with efficiency improvements from the labyrinth seal to brush seal, the HBS results in more judicious usage of fuel and a lighter rotor. The HBS design incorporates cantilevered pad elements to the bristle matrix. Wire EDM spring elements connect the pads to the outer ring, and the bristle tips contact the outer surface of each pad to prevent air passage through the seal. Figure 3 shows the seal with the bristle pack on the front side and the cantilevered pads on the back side. During operation, the arctuate pads result in the formation of a hydrodynamic film. The low radial stiffness of the cantilever pads and bristles allows the pads to lift. The generation of a gas film

results in a relatively low level of leakage while preventing contact between the rotor and seal.

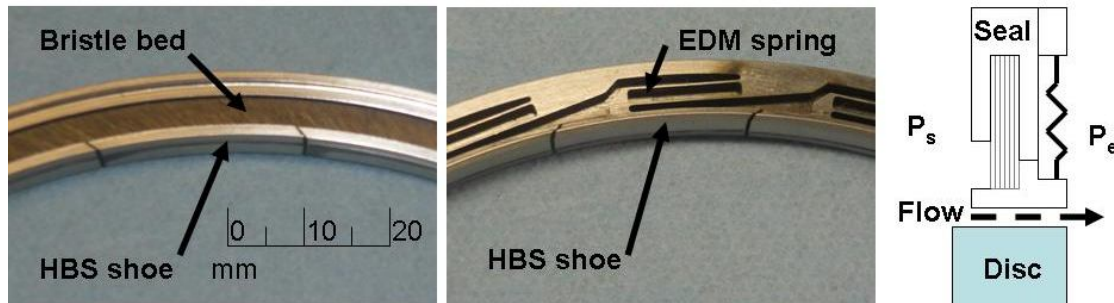


Figure 3: Upstream (left) and downstream (right) view of a HBS with brushes on the upstream and the cantilever pads on the downstream side.

San Andrés et al. [6] experimentally find, that upon pressurization, the fluid film greatly reduces the torque required to overcome any interference between the seal and rotating component. This prevents thermal instability such as that in standard brush seals. Further, the pads ability to move in the radial direction during operation means the HBS does not require the precision manufacturing tolerances associated with labyrinth seals [5]. The cantilever pad elements also add considerable axial stiffness to the seal [6], thus allowing for operation at higher differentials than with standard brush seals.

Rotordynamic tests in Ref. [20] show that the HBS does not excite rotordynamic instability. Delgado and San Andrés [21] find that the bristle-to-bristle and bristle-backplate contact found in both conventional brush seals and a shoed-brush seal produces a stick-slip motion regime. A shoed-brush seal is similar to a HBS only without the spring backing elements. By extension, it is expected that the HBS would experience a similar stick-slip motion. Therefore, a certain load limit must be reached before the excitation of the rotor occurs. Delgado and San Andrés [21] use a combined structural damping and dry friction coefficient to model the mechanical energy dissipation of a cantilever shaft system with a brush seal on the free end of the shaft. Baker [22] finds the HBS dry friction is between 0.51-0.69 depending on the supply pressure imposed.

Additionally, some degree of viscous damping may be present as a result of the generation of a hydrodynamic film under the pads [5].

Delgado et al. [20] predict the rotordynamic force coefficients for a shoed-brush seal. They find that the seal coefficients are fairly independent of operating clearance and supply pressure. Further, they show that the whirl frequency ratio (WFR) is much lower than 0.50 for most rotor speeds. This implies stable operation well beyond twice the first rotor-bearing system critical speed. Baker [22] extends rotordynamic measurements to the HBS for operating at ambient temperature and shows predictions that closely match the real equivalent stiffness and damping.

It is imperative to continue the evaluation of the performance and stability of the sealing methods. By increasing temperature, supply pressure, and rotational speed, the test conditions are able to better match those of a typical gas turbine.

CHAPTER III

HIGH TEMPERATURE TEST APPARATUS

Seal Test Rig

Figure 4 displays the high temperature annular seal test rig with its major components labeled. The test rig contains a pressurization cylinder. In the front side of the cylinder, a disc connected to a shaft rests within a test seal. On the other side, a quill shaft passes through the chamber to a DC motor (90 V, 9.4 A) via a flexible coupling.

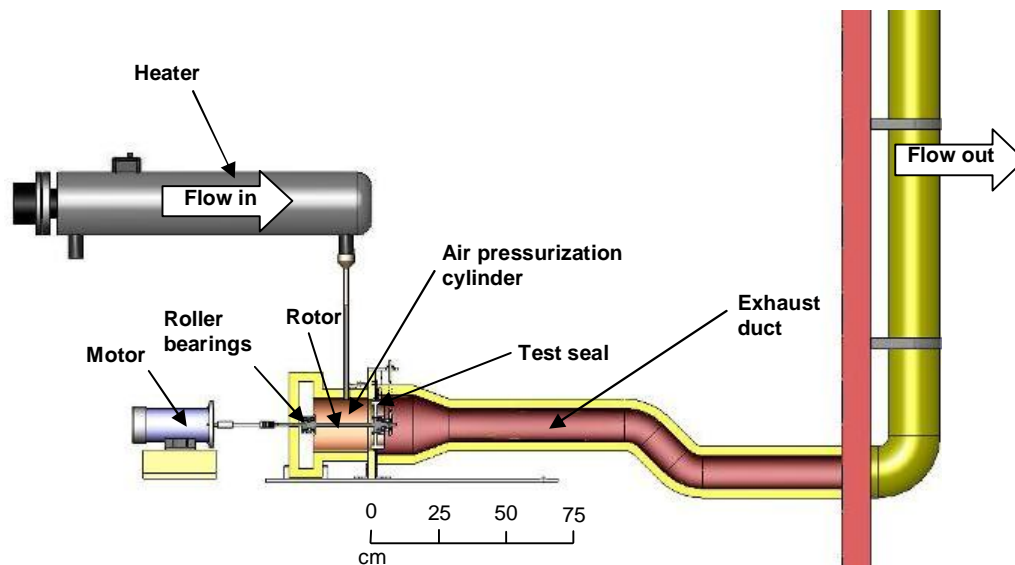


Figure 4: High temperature seal test rig with major components.

Pressurized air (max ~ 8.6 bar) passes through a particle and coalescing filter to remove any water or oil in the air. The supplied air then travels past a flow meter that records the volumetric flow rate. The air pressure is measured immediately afterward. With this information, the volumetric flow rate for a specific pressure and temperature may be transferred into a mass flow rate at standard air conditions. Details on the calculation of the flow rate at various pressures can be found in Appendix A. The air

then flows through an electromechanical control valve and to an electric heater (12 kW, 240 V). The heater warms the air to the desired temperature (max 300 °C) up to the maximum flow rate of 8.6 bar. The hot pressurized air then passes to the pressurization cylinder where both the inlet temperature and pressure into the seal are recorded. Appendix B contains the calibration data for the three pressure sensors used.

Controls for the valve and heater, as well as the data acquisition (DAQ), are set up using a Field Programmable Gate Array (FPGA). This system allows for robust control and reconfiguration of the control and acquisition process through a single cable connection. A Virtual Instrument (VI) allows a user to interface with the rig to control the temperature and pressure in the chamber. The VI then records and saves the desired data upon request. Appendix C discusses the user interface for data acquisition and control.

Figure 5 presents the cross-section view of the pressurized air cylinder and drive motor. Two tapered roller bearings support the overhung shaft and disc inside of the pressurization chamber (Ref. Figure 6). Horizontal and vertical soft coil springs connect the shaft-disc assembly to an external frame. By changing the level of tension in these springs, the disc moves with respect to the stationary seal. Two fiber optic sensors, orthogonally positioned, measure the radial displacements of the disc. Calibration for the fiber optic sensors is presented in Appendix D.

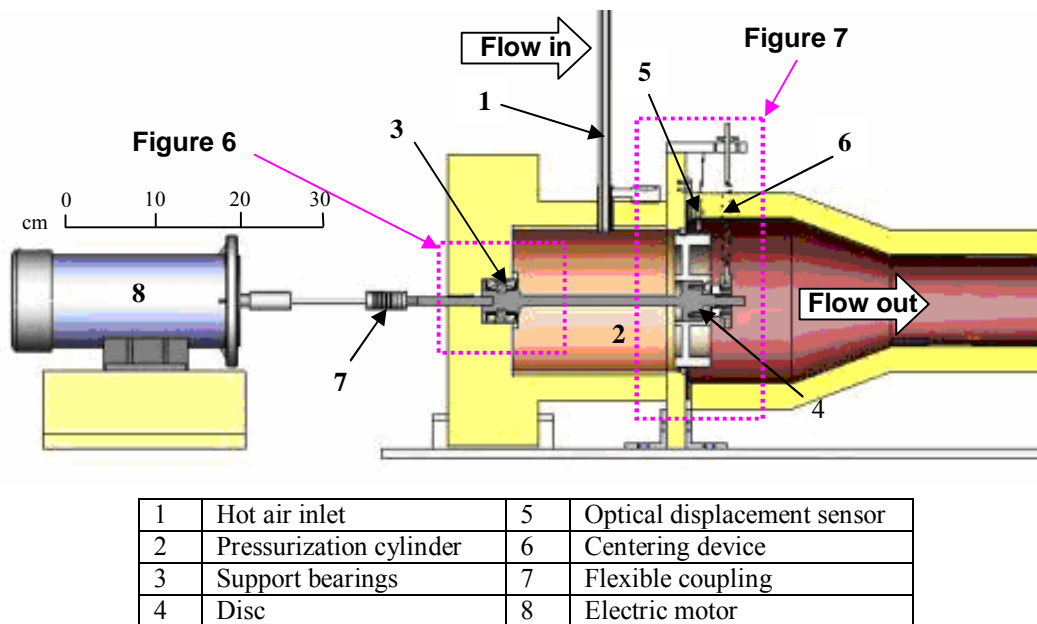


Figure 5: Cutaway view of the pressurization cylinder with instrumentation.

Figure 6 presents the shaft support in greater detail. The tapered roller bearings are packed with Krytox 240-AC, a high temperature grease. Both of the inner bearing rings are press fit onto the shaft. One of the outer bearing races is pressed into a hole inside the pressure chamber. The other outer bearing race is pressed into a retainer that is bolted to the chamber. The tapers of the roller elements are in opposite directions. With this arrangement, the shaft can withstand thrust loads in both axial directions. When the cylinder is pressurized, the pressure on the disc creates a push force in the axial direction. An aluminum silicate plate surrounds the outer bearing to prevent the heating of the area around the bearings. The quill shaft is bolted to the main shaft and connects to the DC motor.

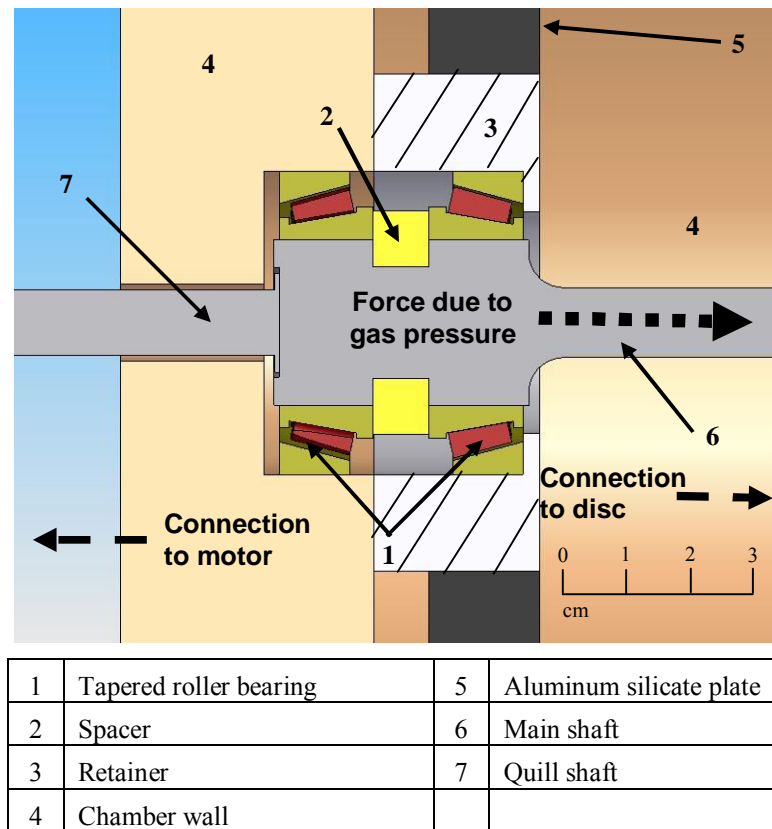


Figure 6: Cutaway view of the shaft support with tapered roller bearings.

Figure 7 shows a detailed view of the disc and centering system within the test rig with one horizontal spring removed for rotordynamic measurements. Accurate leakage measurements depend upon the disc being centered with respect to the test seal. Due to the flexibility of the cantilever shaft, the disc displaces in the vertical direction because of its own weight. One vertical and two horizontal stainless steel coil springs (stiffness~5,870 N/m \pm 2.0) aid to position the disc without the seal enclosure. The springs only work in tension and are relatively soft compared to the stiffness of the tapered roller bearings.

Two fiber optic sensors measure the displacements of the disc surface in the horizontal and vertical directions. In order to locate the center of the disc, the disc is allowed to settle into its minimum vertical position. Then, the vertical spring raises the disc until it reaches its highest point. The average distance from the vertical fiber optic

sensor represents the vertical midpoint. With the disc placed at the vertical midpoint, the procedure is repeated to locate and position the horizontal midpoint. Additionally, the fiber optic sensors are used to measure the seal clearance before and after operation.

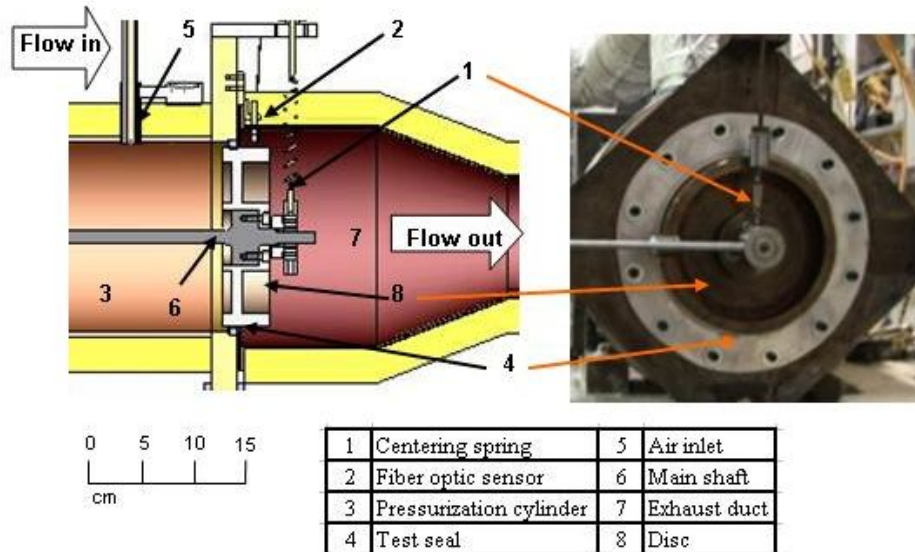


Figure 7: Cutaway view on disc centering system with fiber optic displacement sensors.¹

An electro-magnetic shaker is installed to impart dynamic loads to the disc and seal system. The shaker is softly supported by four cables from the test cell ceiling. The base of the shaker is connected to a steel plate via bungee cords to prevent the shaker from rotating during testing. Figure 8 shows the shaker with connection to the shaft. The exhaust duct is not in place to reveal the shaker connection to the bearing cartridge. The shaker connects to a long stinger rod with a load cell located on the axis of excitation to measure the force input. The force input is exactly along the horizontal axis, parallel to one of the optical sensors and perpendicular to the other. The stinger threads into the same bearing housing used for centering rotor with respect to the seal.

An analog signal is sent to the power amplifier of the shaker. The output from the amplifier powers the shaker. A load cell located on the stinger measures the amplitude

¹ Second horizontal spring removed in Figure 7. See Figure 13 for view with both springs.

and frequency of the force from the shaker. The two high temperature optical sensors measure the displacement of the disc in the horizontal and vertical directions. The signals from the optical sensors and the load cells are sent to the data acquisition system after undergoing the necessary signal conditioning.

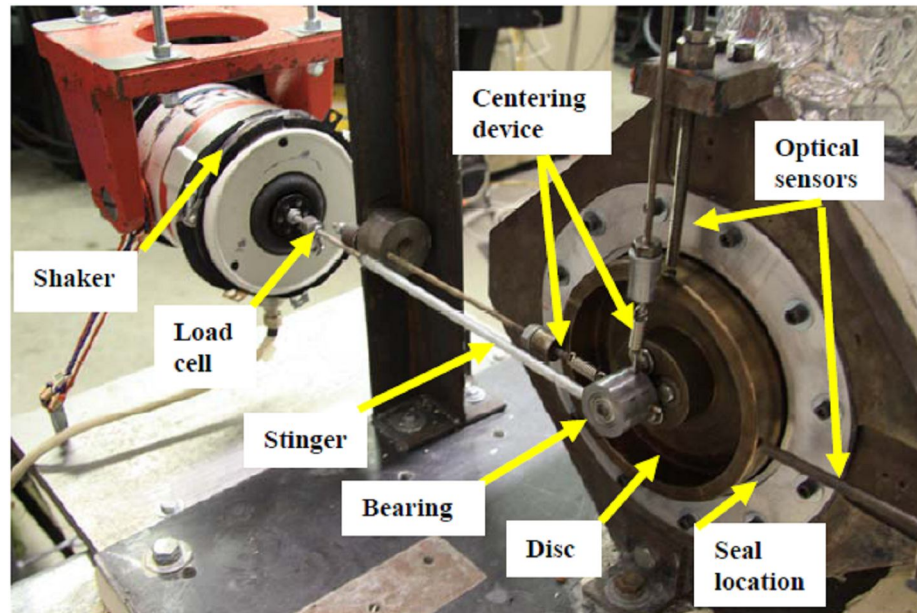


Figure 8: Soft mounted shaker connecting to shaft via load cell and stinger.

Test Seals

Measurements of leakage, wear, and vibration characteristics are performed for three seals: a three-teeth labyrinth seal, a conventional brush seal, and a HBS. Table 1 presents the major dimensions and material properties for the test seals. Each test seal sits in a circumferential groove in the steel air pressurization chamber. The outer diameter of the seal is designed to be hand pressed into the inner diameter groove. The seal is then held in place by a plate bolted to the chamber in 12 places.

The three-teeth labyrinth seal is made of a single aluminum ring. The labyrinth seal has an operating clearance of 1.04 mm diametric (0.52 mm radial) between the tip of the

teeth and the rotor surface at ambient temperature (30°C). The labyrinth seal is slightly longer in the axial direction than the brush seal and HBS.²

The conventional brush seal is composed of a bristle matrix sandwiched between two steel rings. The bristles are made of Haynes-25, a composite material with good wear characteristics. Upon installation, the brush seal has a clearance of 0.52 mm diametric (0.26 mm radial) at ambient conditions. Upon pressurization, the brush seal has been well-documented to experience a blow down effect during which the bristles move radially inwards toward the rotor [3]. This effect drastically lowers the clearance and likely causes contact between the tips of the bristles and the rotor surface [13].

The HBS shares many design properties with the conventional brush seal such as: bristle material, bristle axial length, lay angle, and bristle density. The HBS also has the same clearance as the conventional brush seal at ambient condition. Since both seal rings are made of similar steel, the expansion at high temperature should not change from one seal with respect to the other. Note that in order for the clearances to be the same, the HBS uses a disc with a slightly smaller diameter (<2 mm) made of the same material. This slight difference in diameter does not cause any significant differences to the disc surface speed or thermal growth modeling. The largest differences between the properties of the HBS and the conventional brush seal are due to the addition of the spring EDM elements and the pads. Due to the presence of these features, the HBS has a longer total axial length.

² The labyrinth seal is initially designed to have a 0.20 mm diametric clearance at high temperature (300°C) due to thermal expansion toward the inner radius of the aluminum seal.

Table 1: Test seals-geometry and material properties

Seal Properties	Labyrinth seal	Brush seal	HBS
Seal ring material	Aluminum	Steel	Steel
Seal ring coefficient of thermal expansion	$23.6 \cdot 10^{-6} / ^\circ\text{C}$	$12 \cdot 10^{-6} / ^\circ\text{C}$	$12 \cdot 10^{-6} / ^\circ\text{C}$
Outer diameter	183.2 mm \pm 0.013	183.1 mm \pm 0.013	183.1 mm \pm 0.013
Inner diameter	167.85 mm \pm 0.013	167.33 mm \pm 0.013	166.0 mm \pm 0.013
Seal axial length	8.40 mm \pm 0.013	3.30 mm \pm 0.013	7.87 mm \pm 0.013
Bristle material	Three teeth	Haynes-25	Haynes-25
Bristle coefficient of thermal expansion		$13.5 \cdot 10^{-6} / ^\circ\text{C}$	$13.5 \cdot 10^{-6} / ^\circ\text{C}$
Bristle pack width		1.27 mm \pm 0.013	1.27 mm \pm 0.013
Bristle lay angle		45°	45°
Bristle density (circumference)		850 bristle/ cm	850 bristle/ cm
Rig Properties			
Disc material	4140 Steel	4140 Steel	4140 Steel
Coefficient of thermal expansion	$11.2 \cdot 10^{-6} / ^\circ\text{C}$	$11.2 \cdot 10^{-6} / ^\circ\text{C}$	$11.2 \cdot 10^{-6} / ^\circ\text{C}$
Disc outer diameter (OD)	166.81 mm \pm 0.013	166.81 mm \pm 0.013	165.48 mm \pm 0.013
Disc length	←————→	44.45 mm \pm 0.013	————→
Disc mass	←————→	3.55 kg \pm 0.0004	————→
Shaft length	←————→	447 mm \pm 1.0	————→
Shaft mass	1.13 kg \pm 0.0004	1.13 kg \pm 0.0004	1.13 kg \pm 0.0004
Ambient Clearance (T=30°C)			
OD – ID _s = seal diametral clearance	1.04 mm \pm0.026	0.52 mm \pm0.026	0.52 mm \pm0.026

CHAPTER IV

LEAKAGE MEASUREMENT IN A THREE-TEETH LABYRINTH SEAL

Labyrinth seals provide flow resistance without contacting the rotor. Figure 9 shows a drawing of the test three-teeth labyrinth seal with dimensions. The nominal (radial) clearance of the test seal is ~ 0.52 mm at room temperature. Measurements varying the air supply pressure, air inlet temperature, and rotor speed characterize the labyrinth sealing performance. It is critical that operation not result in hard contact between the seal teeth and the rotor. Contact could lead to wear and thermal distortion of the shaft. This could have deleterious effects on the leakage performance and safety of the test rig. In the measurements, the pressure ratio, P_s/P_e , relates the supply pressure (P_s) to the exhaust pressure (P_e).

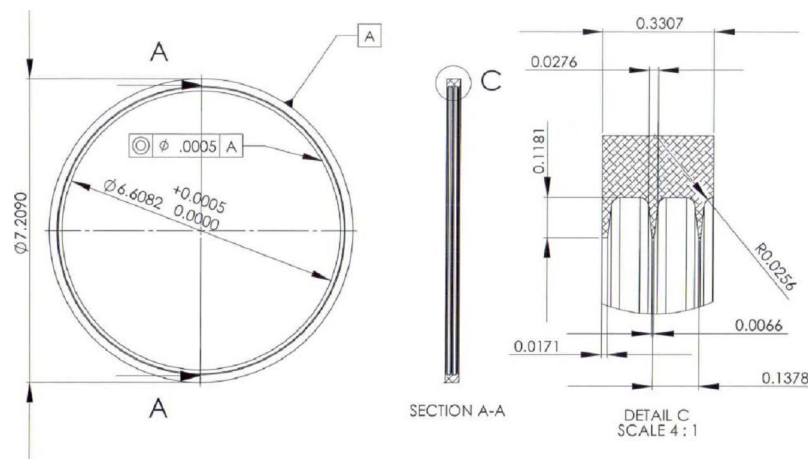


Figure 9: Dimensions of three-teeth labyrinth seal for leakage measurements.

Experimental Procedure

Table 2 shows the air pressurization cylinder temperature and shaft rotational speed for the labyrinth seal tests. At each of the 16 unique test conditions, the air control valve, initially closed, is gradually opened until achieving the maximum flow rate. At each

valve position, a custom data acquisition system records the pressures, temperatures, and flow rate. Five test runs were performed to measure the leakage across the three-teeth labyrinth seal for each of the test conditions.

Table 2: Pressurized cylinder air temperature and shaft speed for labyrinth seal leakage tests

Air temperature [°C]	Shaft rotation [RPM]
25	0
100	1,000
200	2,000
300	3,000

Results and Discussion

During a test condition (fixed air inlet temperature and rotor speed), the procedure records the leakage and inlet pressure five separate times. Figure 10 presents the collection of recorded mass flow rate versus pressure ratio (P_i/P_e) for increasing gas temperatures at the maximum shaft speed of 3,000 RPM (27 m/s). Note that the seal leakage decreases with increasing gas temperature since the density of the air decreases. Table 3 presents the measurement uncertainty for the labyrinth seal measurements. The average uncertainty is at or less than 0.5% of the measured value for both the mass flow rate and the pressure ratio.

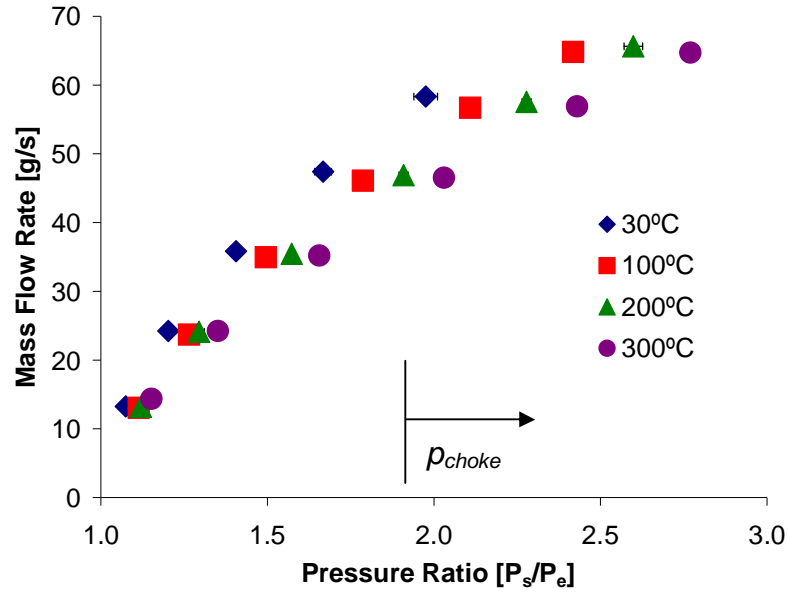


Figure 10: Mass flow rate for three-teeth labyrinth versus pressure ratio for various inlet gas temperatures (30-300°C). Rotor speed at 3,000 RPM.

Table 3: Uncertainty for pressure ratio and mass flow rate in labyrinth seal

	Maximum %	Average %
Pressure ratio	4.4	0.5
Mass flow rate	4.5	0.4

Delgado and Proctor [23] present seal leakage measurements in terms of a flow factor Φ . In this manner, the authors compare the performance of seal types with different diameters, air temperatures, and upstream pressures. The flow factor is defined as

$$\Phi = \frac{\dot{m}\sqrt{T}}{P_s D} \quad (1)$$

where \dot{m} is the seal mass flow rate [kg/s], D is the disc diameter (seal ID), and P_s is the air supply pressure [Pa] at inlet temperature T [K]. Note that the modified flow factor has physical units equal to $\text{kg}\cdot\text{K}^{0.5}/(\text{MPa}\cdot\text{m}\cdot\text{s})$.

Figure 11 displays the derived flow factor Φ for the three-teeth labyrinth seal, using the measurements in Figure 10, versus pressure ratio for increasing gas inlet

temperatures. As expected, the flow factor Φ is not a strong function of the gas temperature. The flow factor increases linearly for small to moderate pressure ratios. Once the flow becomes choked ($P_s/P_e > 1.89$), the flow factor is independent of supply pressure; i.e. the seal mass flow rate is proportional to the upstream (supply) pressure only. The flow factor Φ will serve to compare the leakage performance of the labyrinth seal to the other test seals.

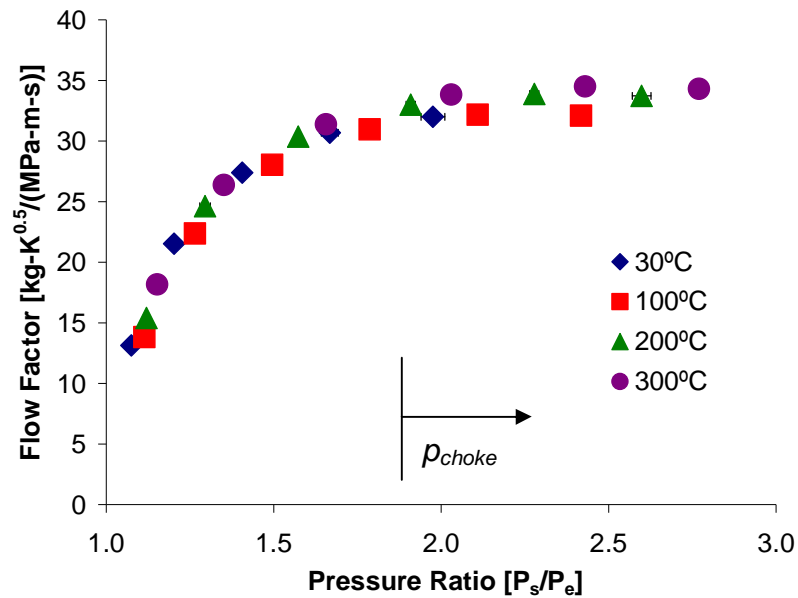


Figure 11: Flow factor Φ for three-teeth labyrinth seal versus pressure ratio (supply/exhaust) for varying inlet temperatures (30-300°C). Rotor speed at 3,000 RPM.

Figure 12 shows the mass flow rate versus rotor speed for operation with air at inlet temperature of 300°C. For the labyrinth seal, the shaft rotation has no noticeable impact on the leakage (axial flow) at any of the three pressure ratios shown. The results are expected since leakage in a labyrinth seal does not explicitly depend on the flow circumferential velocity as noted by Childs [7]. Note that at 3,000 RPM the rotor disk surface speed is just ~ 27 m/s. At such low rotor speeds, centrifugal growth of the disc is insignificant; hence not affecting the operating clearance.

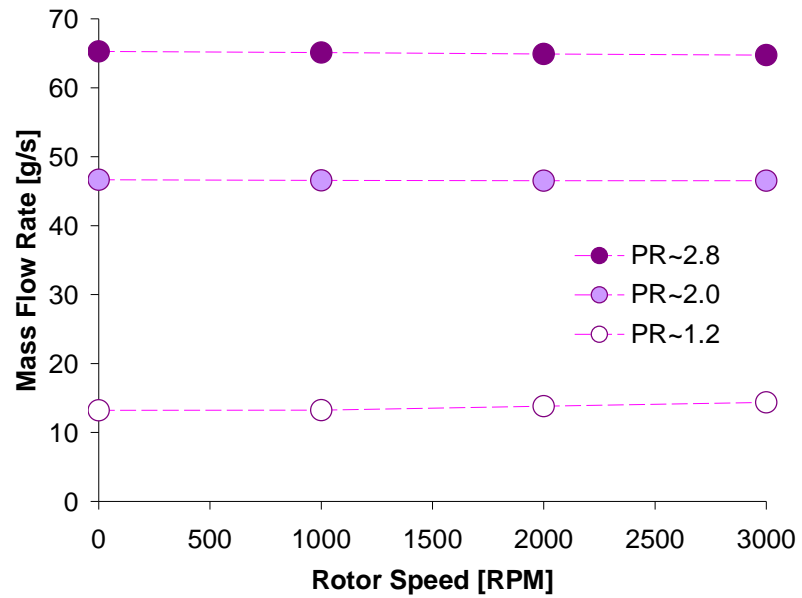


Figure 12: Mass flow rate for three-teeth labyrinth seal versus rotor speed at three pressure ratios ($PR=P_s/P_e=1.2, 2.0, 2.8$). Air inlet temperature of 300°C.

CHAPTER V

MEASUREMENTS OF CLEARANCE AND LEAKAGE

PREDICTIONS FOR A TEST THREE-TEETH LABYRINTH SEAL

Temperatures in rotating machines may exceed 600°C in industrial gas turbines. High temperatures can affect the safety of turbomachinery through wear and bowing of components due to rub. Additionally, increasing the operating temperature causes thermal growth of all of the components inside the engine. Since both rotating and non-rotating components are growing to some degree, clearances may also increase or decrease based upon the design of the engine. For both safety and efficiency reasons, it is critical to quantify the effect that high temperatures have on sealing efficiency.

Measurements of the actual clearance evidence the thermal growth of components. The information can be used to predict overly tight clearances that may cause damage to the rotor or seal teeth. Accurate clearance measurements are also critical to predicting the leakage through the seal using a labyrinth seal fluid flow model.

Experimental Procedure

Figure 13 displays the optical sensors (horizontal and vertical) facing the rotor (disc). The figure also shows the spring and threaded rod devices for centering the disc with respect to the labyrinth seal. The clearance measurement is made during a non-rotating condition for safety reasons. Therefore, the change in clearance only accounts for thermal growth, not centrifugal.

To measure the clearance, the disc is moved to the centered position using the centering device. From the centered position, the operator pulls the disc horizontally until it contacts the teeth along the side of the seal. Then the operator pulls the disc until it contacts the teeth on the opposing horizontal side of the seal. The difference between

the two distances represents the seal diametric clearance. The procedure is repeated three times to ensure accuracy.

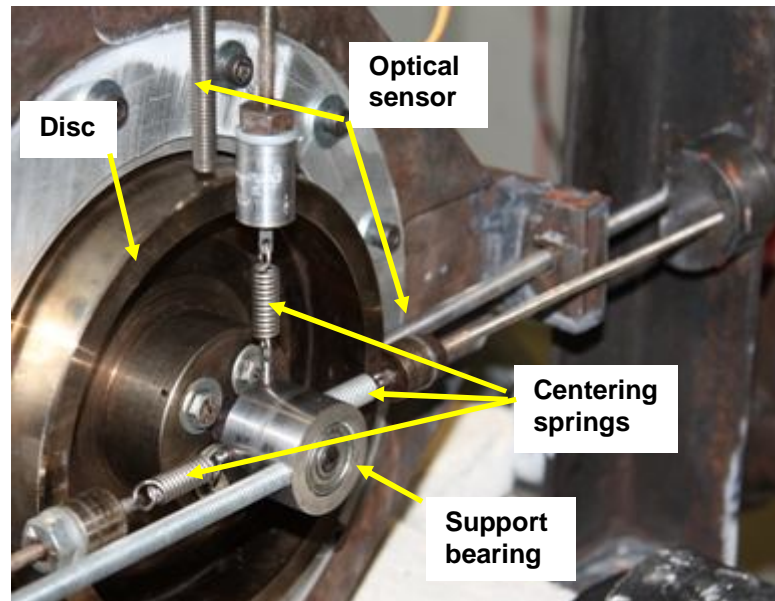


Figure 13: Seal centering device and optical sensors for measuring gap in horizontal and vertical directions.

To measure the temperature of the aluminum labyrinth seal for increasing temperatures, three K-type thermocouples are cold welded onto the downstream face of the seal, the rotor, and the outer surface of the air pressurization housing. The thermocouples connect to the data acquisition board where they can be monitored. The DAQ allows the user to set a desired operating temperature for the air or for the thermocouples on the seal. Once the desired temperature is reached, the heater maintains the temperature until the user specified value changes.

Figure 14 depicts the location of the thermocouples as viewed from the downstream (low pressure) side of the seal. Additionally, measurements of the seal clearance as well as the air inlet pressure are conducted for a constant mass flow rate (as set by the electromechanical control valve).

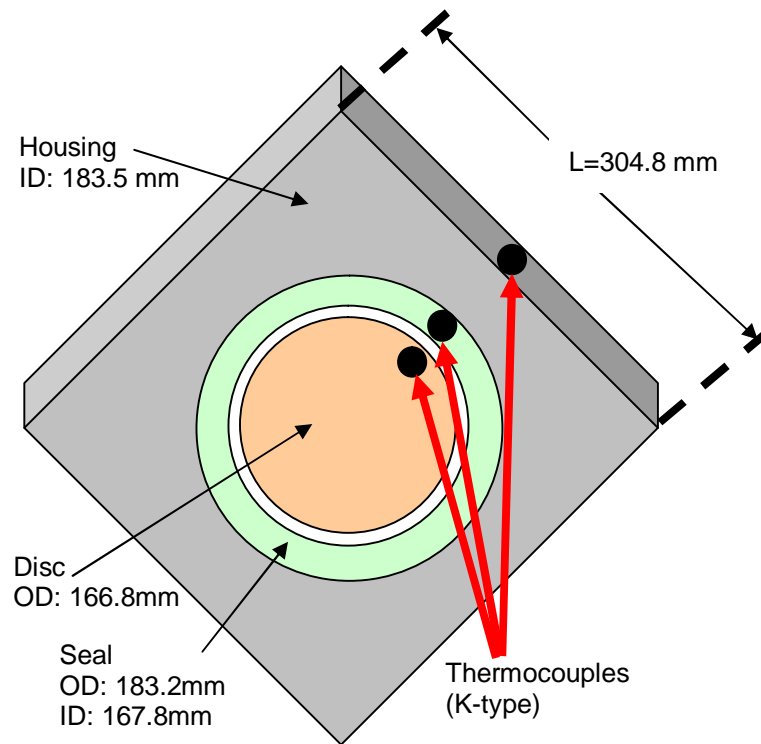


Figure 14: Location of thermocouples viewed from the downstream end (low pressure side) with exhaust duct removed. Thermocouple on housing is located on the outer surface of housing (exposed to ambient air).

Results and Discussion

Figure 15 presents the recorded temperature of the inlet air and test rig components versus time. In the tests, the air inlet temperature is fixed (100 °C, 200 °C and 300°C) as the gas flows through the test seal. The control system keeps a constant flow rate; and hence, the upstream pressure varies as the temperature increases. Note how the test system (disc, seal and housing) takes nearly one hour to reach a steady state condition for each inlet temperature. At the highest air temperature (300°C), the test rig requires the longest time to reach a steady state condition. The thermal (inertia) lag is most evident at the rig housing. There is a significant temperature gradient along the radial direction moving outwards from the disc with the housing reaching nearly 80°C less

temperature at the highest inlet air temperature. The changes in temperature also denote uneven thermal growth of the components.

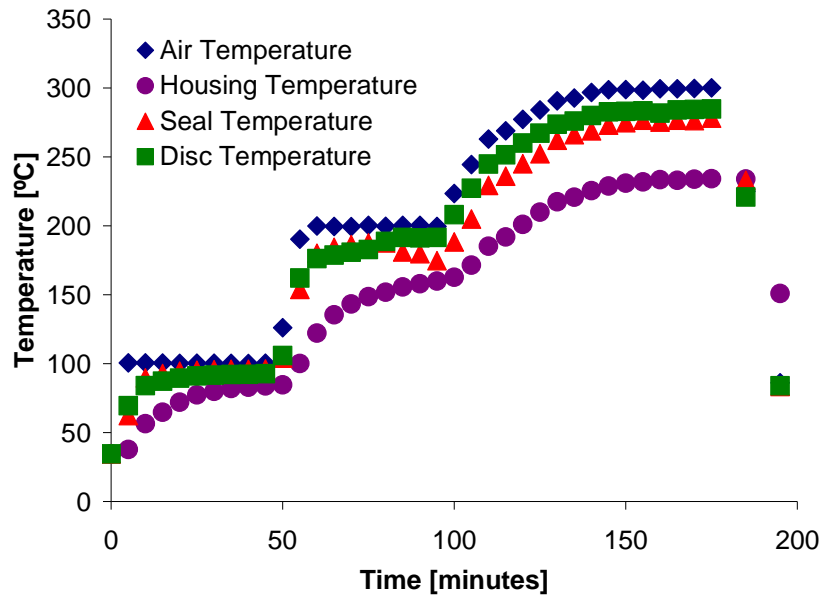


Figure 15: Temporal evolution of temperatures at various locations in test rig for three-teeth labyrinth seal. Constant air flow at 35 g/s. Air inlet temperature vs. time specified.

Figure 16 displays the measured air inlet temperature and the diametral clearance in the three-teeth labyrinth seal. Clearance measurements are made using the disc centering mechanism and are performed under non-rotating shaft conditions. Note that even at elevated air temperatures (300°C) the diametral clearance does not deviate greatly from the nominal value of 1.04 mm at ambient air temperature (30°C).

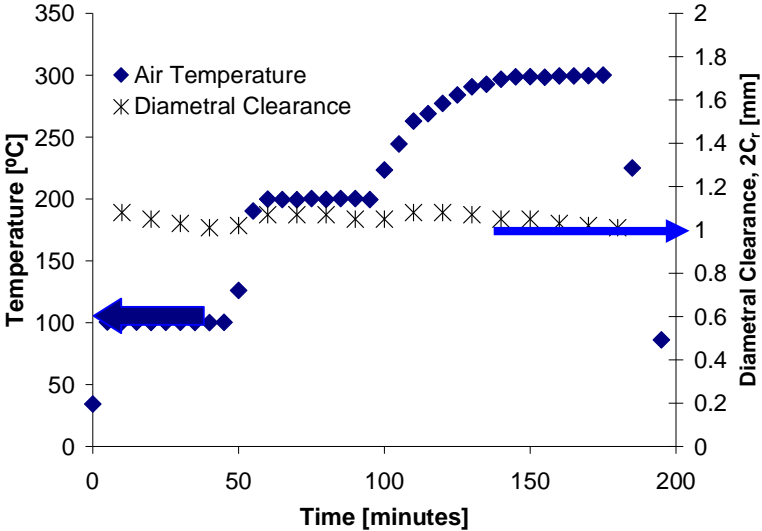


Figure 16: Temporal evolution of diametral clearance and air inlet temperature (nominal clearance of 1.04 mm at room temperature) in three-teeth labyrinth seal. Operation with constant flow at 35 g/s. No shaft rotation.

Figure 17 displays the measured air supply (gauge) pressure along with the air inlet temperature versus time. As the density of the air increases with temperature, the supply pressure increases to maintain the same mass flow rate through the seal.

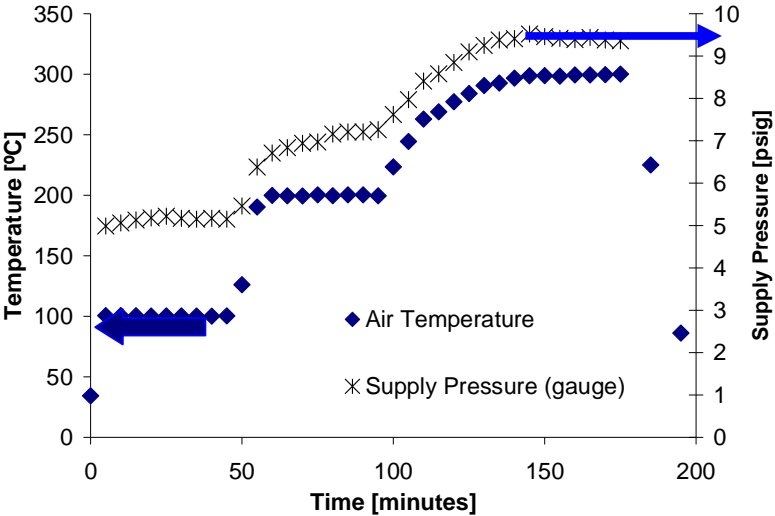


Figure 17: Temporal evolution of supply pressure and air inlet temperature and in three-teeth labyrinth seal. Operation with constant flow at 35 g/s.

The measurements in Figure 16 show the clearance to be relatively insensitive to the change in air temperature. In a simple analysis, the thermal growth in (inner or outer) diameter (ΔD) of a component equals

$$\Delta D = \alpha * \Delta T * D \quad (2)$$

where α is the coefficient of thermal expansion of the material [$^{\circ}\text{C}$], ΔT is the change in temperature [$^{\circ}\text{C}$], and D is the initial length of the diameter [m].

Since the coefficient of thermal expansion is greater for the aluminum seal than that for the steel housing ($\alpha_s > \alpha_h$), the difference between the change in the inner diameter of the housing and the growth of the outer diameter of the seal results in an interference fit (IF) between the housing and seal.

$$IF = \Delta ID_h - \Delta OD_s \quad (3)$$

Likewise, the inner diameter of the seal (ID_s) expands due to the increase in temperature. However, the inner diameter also experiences a shrinking due to the interference between the inner diameter of the housing and the outer diameter of the seal. The total change in the inner diameter of the seal is represented by the combination of the thermal growth of the inner diameter and the interference between the seal and housing.

$$\Delta ID_s = \alpha_s * \Delta T_s * ID_s + IF \quad (4)$$

The change in diametric clearance is represented by the difference of the change in the inner diameter of the seal and the change in the outer diameter of the disc (OD_d).

$$\Delta 2C_r = \Delta ID_s - \alpha_d * \Delta T_d * OD_d \quad (5)$$

substituting into Equation 5

$$\Delta 2C_r = \alpha_s * \Delta T_s * ID_s + \alpha_h * \Delta T_h * ID_h - \alpha_s * \Delta T_s * OD_s - \alpha_d * \Delta T_d * OD_d \quad (6)$$

Direct measurements of the seal clearance using feeler gauges aid to validate the most recent ones (see Figure 16). To achieve this task with the test rig still at a high temperature, the bolted connections fixing the exhaust duct are replaced with clamps. With this change, the exhaust can be removed in ~ 20 seconds. Note that no (hot) air

flows through the seal while performing the measurements. The temperature of the components is monitored to ensure that the heated components do not cool significantly from the steady state temperatures.

Figure 18 displays the measured diametral clearance using feeler gauges and the prediction of change in clearance using Eq. 6 for the three-teeth labyrinth seal versus gas inlet temperature with uncertainty listed. The measurements show that the clearance does not vary greatly with temperature, in fact being similar to the clearances presented in Figure 16. Using feeler gauges provides a more accurate measurement method as the gap is directly measured without any of the inaccuracies associated with the centering system. Thus, the diametral gap does not vary significantly from its initial clearance of 1.04 mm.

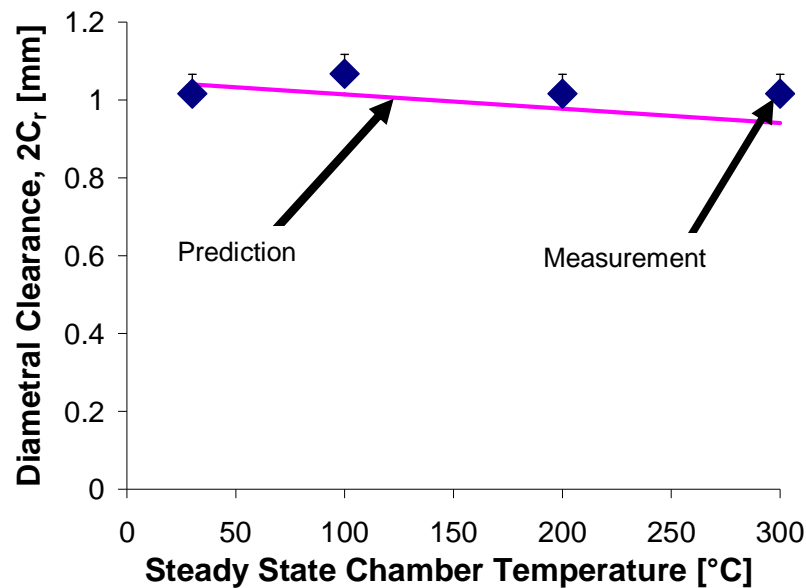


Figure 18: Three-teeth labyrinth seal diametral clearance using feeler gauges and predictions versus gas inlet temperature. No shaft rotation.

The mass flow rate (\dot{m}) through a knife edge in a labyrinth seal cavity is a function of the pressure upstream pressure (P_{i-1}) and the cavity pressure (P_i) [7].

$$\dot{m} = \mu_0 \mu_i A \sqrt{\frac{P_{i-1}^2 - P_i^2}{RT}} \quad (7)$$

where $A = \pi D C_r$ is the flow area for a seal with diameter D and tip radial clearance C_r .

Above, (μ_0) is the kinetic-energy carryover factor from the upstream cavity,

$$\mu_0 = \left(\frac{N_T}{(1-\alpha)N_T + \alpha} \right)^{\frac{1}{2}} \text{ with } \alpha = 1 - \left(1 + 16.6 \frac{C_r}{L} \right)^{-2} \quad (8)$$

L is a cavity axial length, and (μ_i) is the flow coefficient,

$$\mu_i = \frac{\pi}{\pi + 2 - 5\beta_i + 2\beta_i^2} \text{ with } \beta_i = \left[\left(\frac{P_{i-1}}{P_i} \right)^{\frac{\gamma-1}{\gamma}} - 1 \right] \quad (9)$$

For a labyrinth seal composed of a number of cavities (N_T), Equation (7) is recursively used to find the mass flow rate and cavity pressures. The iterative calculation ensures flow continuity through each tooth. The model includes considerations for choked flow that can occur at the exit (last) tooth of the labyrinth seal. Note from the equations that decreasing the clearance lowers the predicted flow rate in two ways. A lower clearance results in a smaller area for the flow to pass. A smaller clearance also decreases the kinetic carryover term. This means that the amount of energy passing to the succeeding cavity will decrease and thus the flow will decrease.

The maximum flow under choked conditions is

$$\dot{m}_i = \frac{p_{choke} \mu_0 P_{i-1} A}{\sqrt{RT}} \quad (10)$$

where $p_{choke} = 0.51$ is the (ambient/upstream) pressure for choked condition in air.

Figure 19 presents the predicted mass flow rate using Equation 7 and XLLaby©, a predictive software for labyrinth seals for operation without shaft rotation. Predictions of mass flow rate compared to two air temperatures equaling 30°C and 300°C. The measured clearances, see Figure 18, are used to predict the mass flow rate. The two analyses produce similar predictions of seal mass flow rate, albeit XLLaby © predicts slightly higher values (~6%) over the range of supply pressures.

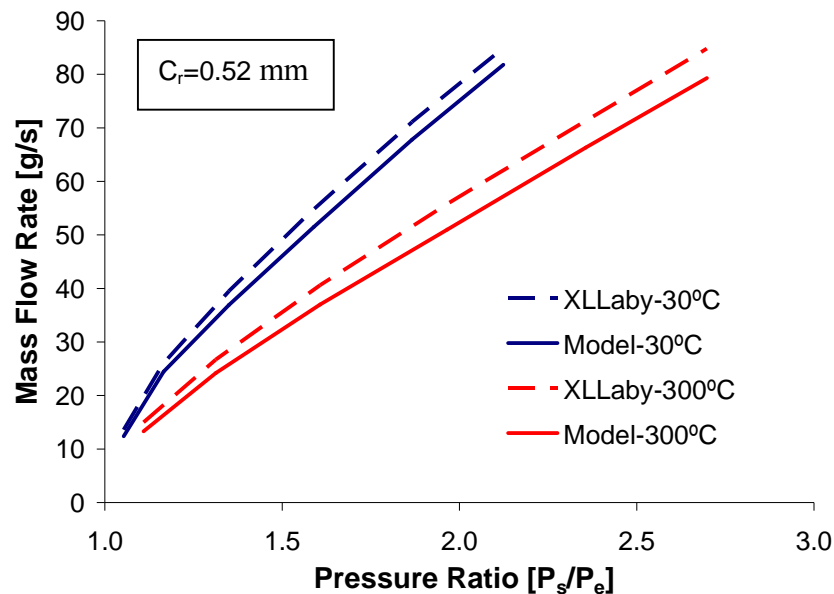


Figure 19: Predicted mass flow rate versus (inlet/exhaust) pressure ratio for three-teeth labyrinth seal using model and XLLaby©. No shaft rotation. Predictions based on measured clearance at 30°C and 300°C (0.52 mm).

Figure 20 shows a comparison of the predicted and measured seal mass flow rates. The predictions implement the measured radial clearance $C_r \sim 0.52$ mm, see Figure 18. The predictions are close to the measured mass flow rate at supply pressures less than 1.7 bar, $\sim 5\%$ error. However, the error increases significantly at higher supply pressures, up to 25%. Since the labyrinth seal clearance does not decrease, as the current measurements evidence, the leakage through the labyrinth seal is higher than originally anticipated. This shortcoming is noted when comparing the different sealing methods, as the labyrinth seal could be designed for a considerably lesser leakage if operating with a lower clearance. On the other hand, note that labyrinth seals with tight clearances are not practical. A too small clearance seal is difficult to assemble, does not tolerate misalignments or large rotor excursions without permanent damage. Inevitably, the seal tight clearance enlarges due to intermittent rubs during start up and shut downs.

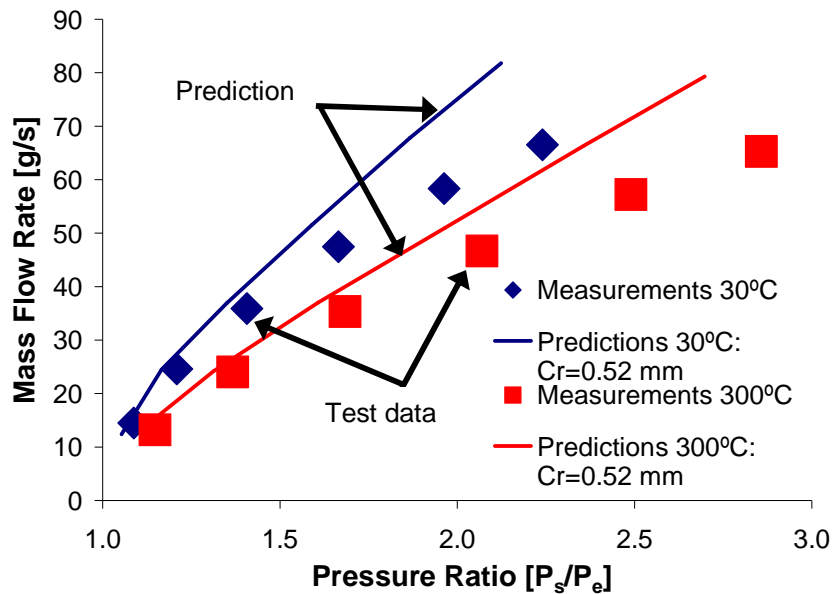


Figure 20: Predicted and measured mass flow rate versus (inlet/exhaust) pressure ratio for three-teeth labyrinth seal at two inlet temperatures. No shaft rotation. Predictions based on two distinct (measured) clearances.

Figure 21 presents the derived flow factor Φ versus pressure ratio for the flow data in Figure 20. Both the predicted and measured flow factors are relatively independent of the air temperature. Further, for supply pressures over 2.0 bar the flow factor Φ approaches a constant magnitude of 30. Once again, for lower supply pressure ($P_s < 1.7$ bar), the predictions slightly overpredict ($\sim 5\%$) the experimentally derived flow factor. At a supply pressure of 1.7 bar, the pressure is 1.42 bar and 1.22 bar in the two seal cavities. The discrepancies in predictions and measurements point out to limitations in the flow model or a seal with uneven clearance (vertical and horizontal).

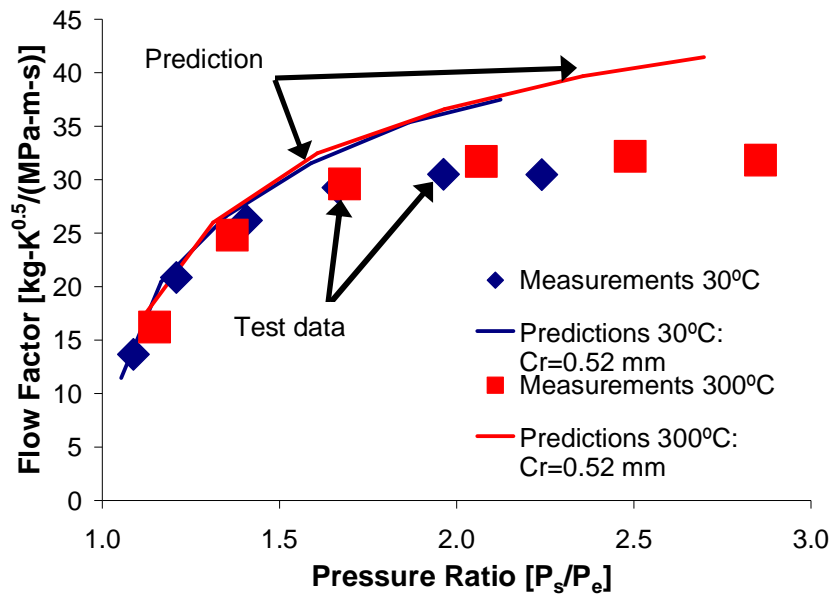


Figure 21: Predicted and experimental flow factor Φ versus (inlet/exhaust) pressure ratio for three-teeth labyrinth seal at two inlet temperatures. No shaft rotation. Predictions based on two distinct clearances.

CHAPTER VI

LEAKAGE MEASUREMENTS IN A CONVENTIONAL BRUSH SEAL

Brush seals inhibit the passage of gas by using a tightly packed area of bristles. These bristles are usually designed to contact the surface of the rotating component upon installation. After sustained operation, the bristles wear thereby decreasing the interference between bristles and rotor. The current test seal is designed with a radial clearance at ambient temperature. Due to bristle blow-down and thermal growth, however, the bristles will contact the rotor surface when operating at high supply pressures and air temperatures.

This chapter details leakage measurements in a conventional brush seal. The measurements are made over a range of supply pressure, air temperature, and rotor speed conditions.

Experimental Procedure

The procedure for measurement of flow rate through the conventional brush seal is identical to the procedure for flow rate measurements through the three-teeth labyrinth seal, as described in Chapter IV. Leakage and temperature measurements are conducted at identical test conditions as those detailed in Table 2. Brush seals are installed with the bristles facing the supply pressure side of the seal and the backing plate facing the exhaust pressured side. By installing the brush seal in this manner, the backing plate prevents the bristles from being pushed in the axial direction due to the pressure differential. If the bristles do buckle when a pressured differential is applied to the seal, the clearance will drastically open allowing for unrestricted flow and thus higher leakage.

Results and Discussion

Figure 22 displays the recorded brush seal mass flow rate versus pressure ratio (P_s/P_e) for varying gas temperatures at a rotor speed of 3,000 RPM. As with the three-teeth labyrinth seal, the brush seal leakage decreases with increasing gas temperature since the operating clearance decreases and the viscosity of air increases. Table 4 presents the measurement uncertainty for the conventional brush seal measurements. The average uncertainty is at or less than 1.3% of the measured value for both the mass flow rate and the pressure ratio.

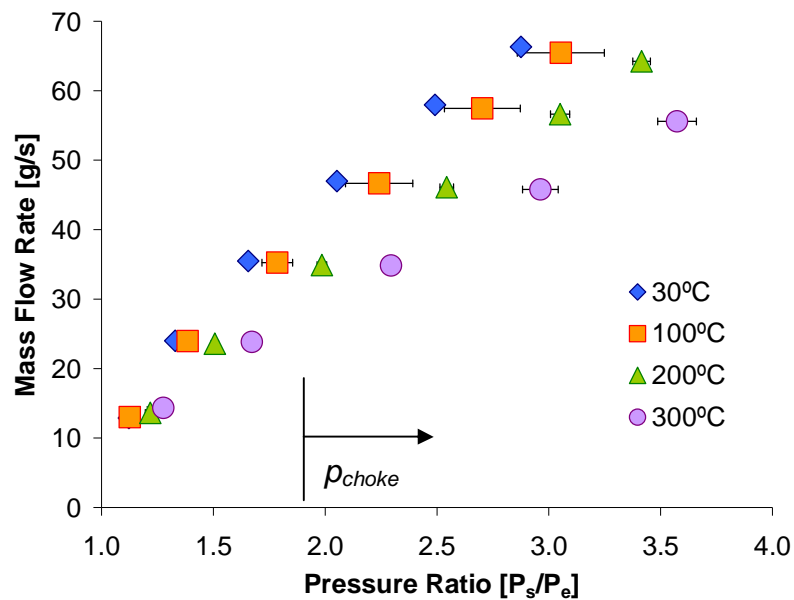


Figure 22: Mass flow rate for conventional brush seal versus pressure ratio (supply/exhaust) for varying inlet temperatures (30-300°C). Rotor Speed at 3,000 RPM.

Table 4: Uncertainty for pressure ratio and mass flow rate in conventional brush seal

	Maximum %	Average %
Pressure ratio	6.7	1.3
Mass flow rate	6.3	0.5

As with the labyrinth seal, the flow factor (Φ) defines the brush seal leakage. Figure 23 displays the flow factor (Φ) for the conventional brush seal versus pressure ratio for increasing gas inlet temperatures. Once the flow is choked ($P_s / P_e > 1.89$), the flow factor becomes independent of supply pressure. The gas temperature has only a slight effect on the flow factor. Between the lowest and highest gas temperatures, the flow factor changes by less than 10%; whereas the physical flow rate decreases by more than 40%. Therefore, the flow factor (Φ) is well suited to compare the leakage between the test seals regardless of gas temperature.

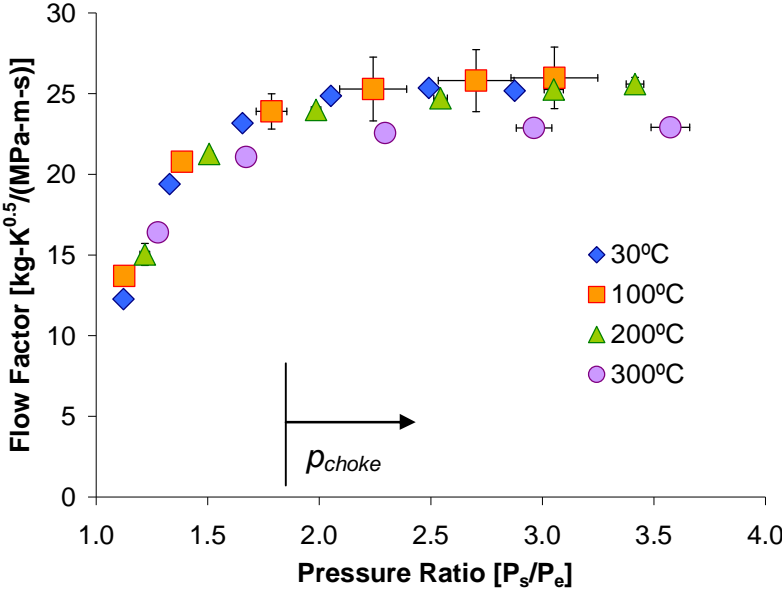


Figure 23: Flow factor Φ for conventional brush seal versus pressure ratio (supply/exhaust) for varying inlet temperatures (30-300°C). Rotor speed of 3,000 RPM.

Figure 24 shows the mass flow rate for the conventional brush seal versus rotor speed for operation with air at inlet temperature of 300°C and three pressurized conditions. The rotor speed has no noticeable effect on the conventional brush seal mass flow rate. As with the labyrinth seal, the only way rotation can decrease the mass flow rate is by centrifugal growth of the rotor. The measurements reaffirm the capability of the brush seal to restrict flow even for moderately high rotor speeds (up to 27 m/s).

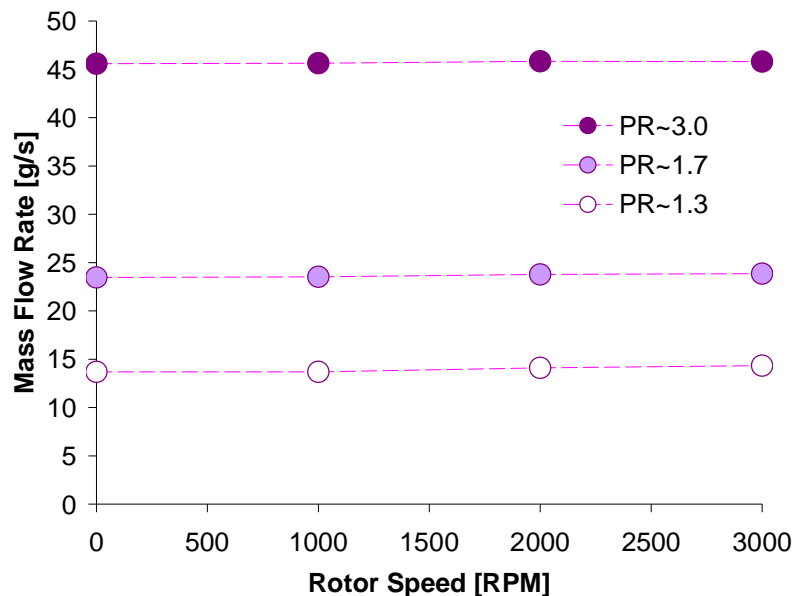


Figure 24: Mass flow rate for conventional brush seal versus rotor speed at three pressure ratios ($PR=P_s/P_e=1.3, 1.7, 3.0$). Air inlet temperature of 300°C.

Chupp and Holle [24] describe a porous type flow model for prediction of mass flow rate through brush seals. The model is highly empirical, and introduces an effective thickness parameter. A worksheet by San Andrés [25] predicts the mass flow rate through brush seals reproducing the porosity model. Figure 25 compares the predicted mass flow rate to the measured leakage for the test brush seal. To obtain the predictions, an effective thickness of ~ 0.912 mm is used. The actual bristle width is 1.27 mm. The effective thickness is used to match the flow rate at the maximum inlet pressure condition. Once the value is found, the flow rate is found for the remaining pressure

conditions. The discrepancy is likely due to the empirical nature of the equation as well as the brush seal operating as a non-contacting seal prior to blow down of the bristles. At low pressure differentials, a region of unrestricted flow exists between the seal and rotor. The clearance drastically increases the mass flow rate.

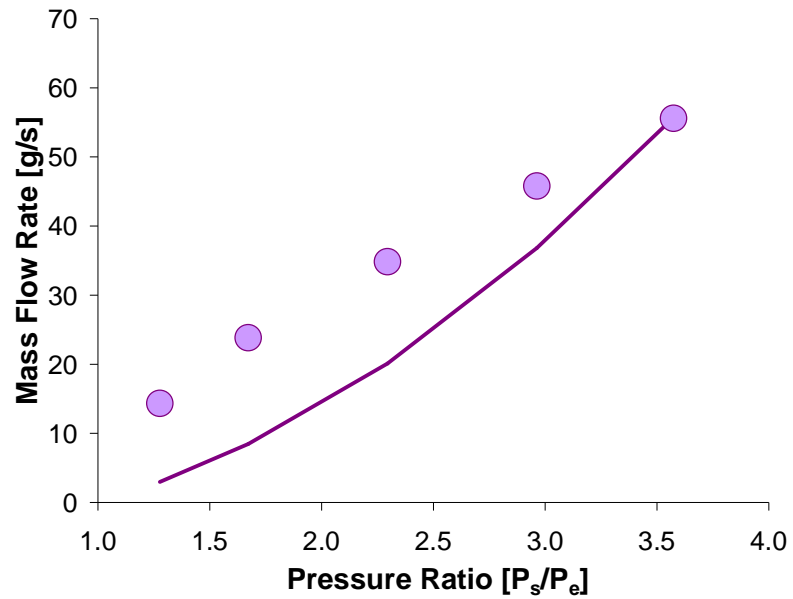


Figure 25: Comparison of predicted and measured mass flow rates in brush seal versus pressure ratio $[P_s/P_e]$. Rotor speed of 3,000 RPM. Air inlet temperature at 300°C. Predictions from model in [25].

CHAPTER VII

LEAKAGE MEASUREMENTS IN A HYBRID BRUSH SEAL

The following chapter details leakage measurements in a HBS. The measurements are made over a range of supply pressure, air temperature, and rotor speed conditions similar to those for the brush seal and three-teeth labyrinth seal. The Hybrid Brush Seal (HBS) prevents the flow of air using a bristle bed matrix similar to that of a brush seal. Additionally, the HBS adds multiple spring supported cantilevered pads. These pads contact the rotor instead of the bristles while the resilient (soft) supports allow for large radial displacements. These springs are much stiffer in the axial direction than in the radial direction. The HBS has a clearance at ambient condition (0.52 mm diametral). As with the brush seal, the HBS then experiences a blow down effect at increasing inlet pressures wherein the bristles and pads move radially inward towards the disc closing its clearance.

Experimental Procedure

The procedure for measurement of leakage through the HBS is nearly identical to the procedure for measurement through the three-teeth labyrinth seal. The HBS is installed with the bristles facing the supply pressure side of the seal and the spring elements facing the exhaust pressured side. The spring elements give the HBS considerable stiffness in the axial direction and prevent the bristles from buckling due to large pressure differentials. As with the conventional brush seal, buckling of the bristles in the HBS will create a large region of unrestricted flow, drastically increasing the seal leakage.

Results and Discussion

Figure 26 shows the measured HBS mass flow rate versus pressure ratio (P_s/P_e) for four increasing gas temperatures to 300°C. Uncertainties bars are shown. As with the

labyrinth seal and brush seal, the mass flow rate reduces as the air inlet temperature increases. Table 5 presents the uncertainty for the mass flow rate and pressure ratio for the HBS leakage measurements. The measurements have an average uncertainty of 0.6% and lower.

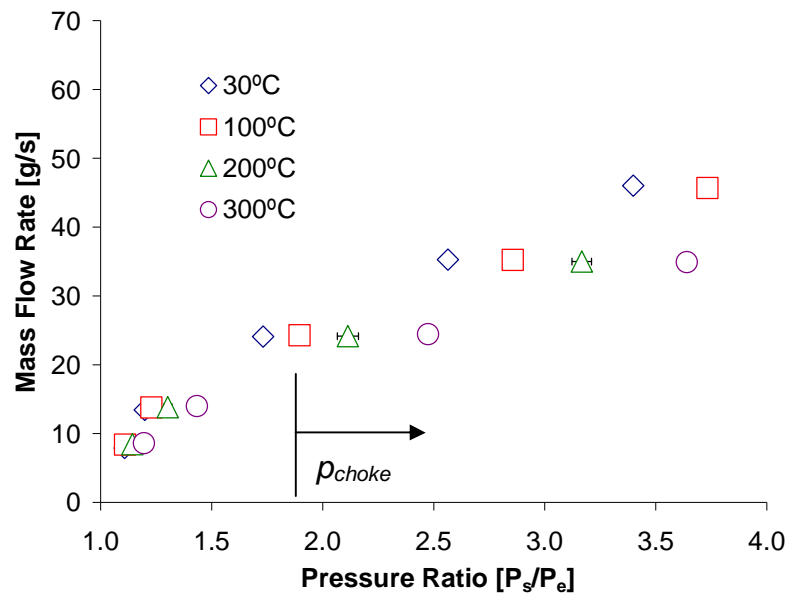


Figure 26: Mass flow rate for HBS versus pressure ratio (supply/exhaust) for varying inlet temperatures (30-300°C). Rotor speed at 3,000 RPM.

Table 5: Uncertainty for pressure ratio and mass flow rate in conventional brush seal

	Maximum %	Average %
Pressure ratio	3.0	0.6
Mass flow rate	2.4	0.5

Figure 27 presents the derived HBS flow factor (Φ) versus pressure ratio for the same test conditions. The flow factor rises slightly, before dropping at a pressure ratio of ~ 1.89 . As with the labyrinth and brush seals, the gas inlet temperature has little influence in the flow factor.

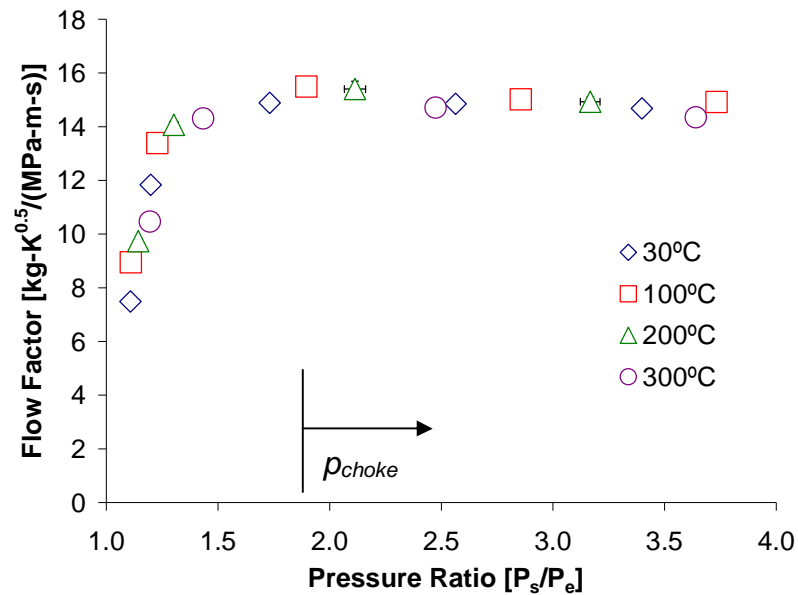


Figure 27: Flow factor ϕ for HBS versus pressure ratio (supply/exhaust) for varying inlet temperatures (30-300°C). Rotor speed of 3,000 RPM.

As with the labyrinth and brush seals, it is desirable to assess how shaft rotation affects the mass flow rate of the HBS. Figure 28 shows the HBS mass flow rate versus rotor speed for three inlet pressures. No noticeable change in mass flow rate is present at any of the pressure ratios. As stated in Chapter IV, higher shaft speeds lead to disk centrifugal growth and reduced clearance that acts to decrease the mass flow rate for a specific seal. For the current relatively low speeds used (< 27 m/s), however, no significant centrifugal expansion is expected.

Baker [22] shows leakage measurements of a HBS at surface speeds approaching 12 m/s (1,350 RPM). The current measurements of flow rate through the HBS leakage performance up to surface speeds of ~ 27 m/s. The leakage is invariant of rotor speed. Further work is necessary to conduct leakage measurements of the HBS at surface speeds typical of gas turbines, an order of magnitude higher than the current measurements.

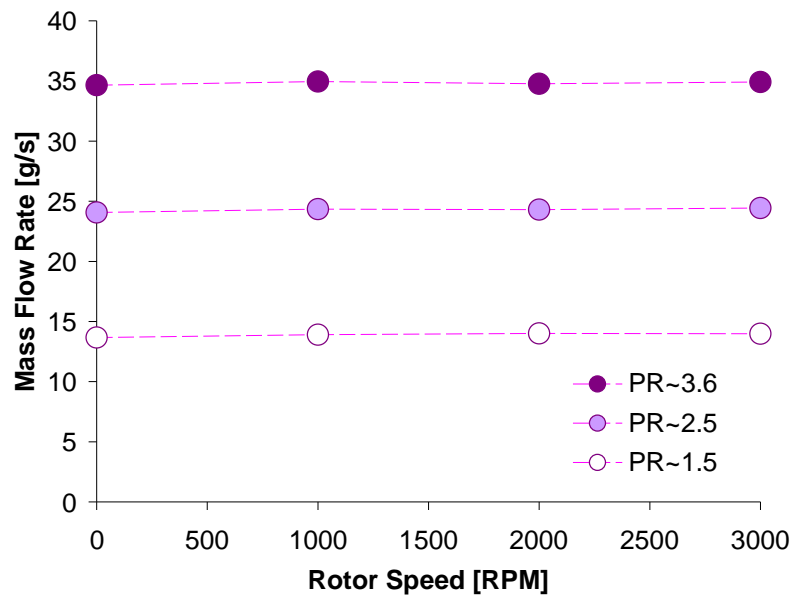


Figure 28: Mass flow rate for HBS versus rotor speed at three pressure ratios ($PR=P_s/P_e=1.5, 2.5, 3.6$). Air inlet temperature of 300°C .

As with the conventional brush seal, a porous media fluid flow model predicts the mass flow rate. Figure 29 compares the predicted mass flow rate to the measured leakage. To obtain the predictions, an effective thickness of ~ 0.88 mm (0.0346 in) is used to match the experimental flow factor at a pressure ratio of 3.6. Note that the flow predictions at lower supply pressures severely under predict the flow rate. If the clearance between the tips of the bristles and the rotor is known, then the model could include a porous model and a model for unrestricted annular flow. The current test rig is not suited to measure blow-down effects and changes in clearance due to thermal growth in radially flexible seals.

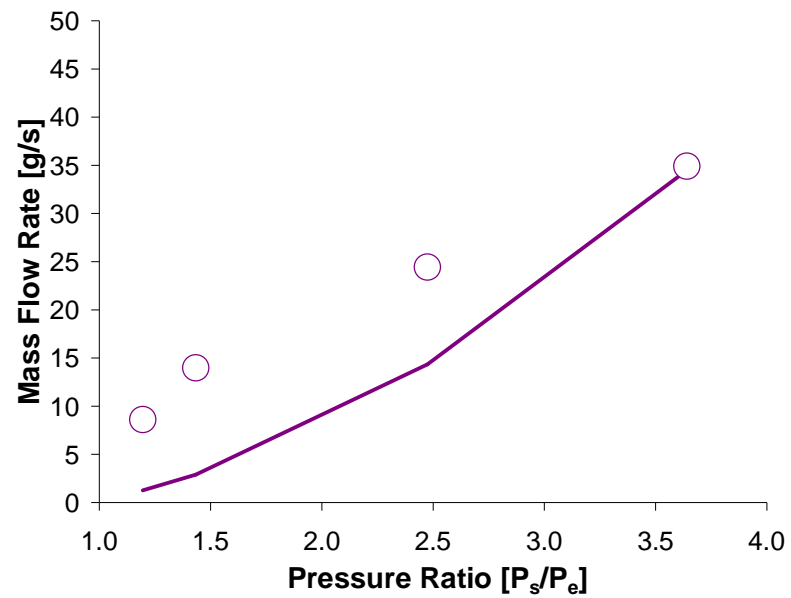


Figure 29: Comparison of predicted and measured mass flow rate in HBS versus pressure ratio [P_s/P_e]. Rotor speed of 1000 RPM. Air inlet temperature at 300°C.

CHAPTER VIII

COMPARISON OF LEAKAGE FOR THREE TEST SEALS

Air temperature and rotor speed have little influence on the test seals' flow factor. Hence, it is sufficient to present measurements of flow factor at a single rotor speed and temperature condition to compare the leakage between sealing methods. Figure 30 displays the test seals' flow factor versus pressure ratio for operation at the highest test temperature of 300°C and rotor speed of 3,000 RPM. Notice the HBS produces the lowest overall leakage (and flow factor). At a pressure ratio of 2.0 and above, the HBS overall leakage is ~ 38% and 61% less than the brush seal and the labyrinth seal, respectively. Since both the conventional brush seal and HBS have the same clearance at ambient condition, the HBS is likely experiencing a greater degree of blow-down upon pressurization due to the addition of pads.

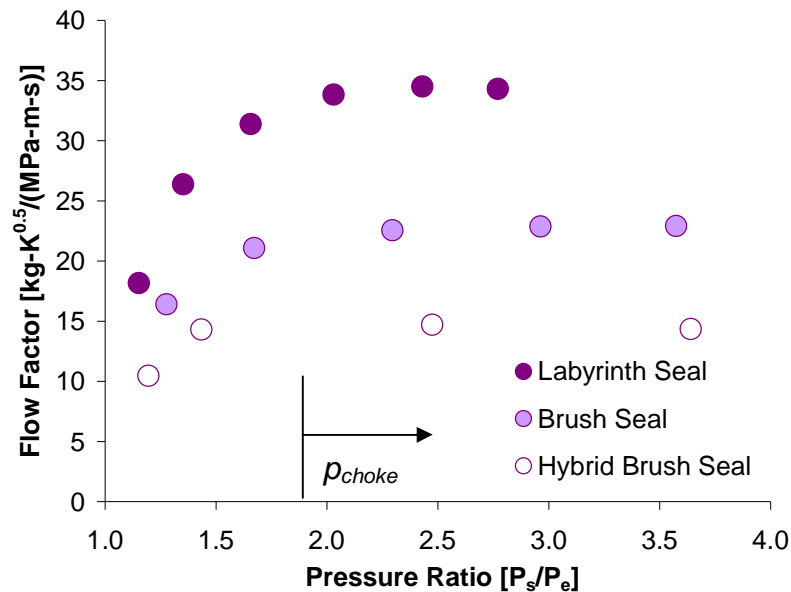


Figure 30: Flow factor Φ for three test seals versus pressure ratio $[P_s/P_e]$. Air inlet temperature at 300°C. Rotor speed at 3,000 RPM.

The seal leakage should be inversely proportional to the axial length (l) of the sealing surface. A modified flow factor Φ_M equals the product of the flow factor Φ times the sealing length l , i.e.

$$\Phi_M = \Phi l = \frac{\dot{m}\sqrt{T}}{P_s D} l \quad (11)$$

Note that the modified flow factor has physical units equal to $\text{kg}\cdot\text{K}^{0.5}/(\text{MPa}\cdot\text{s})$. For the labyrinth seal, its length, $l=8.4$ mm, equals the seal physical length (teeth and cavities). For the HBS and brush seal, the primary region of flow is through the bristle pack, of identical length in both seals. Hence, the BS and HBS sealing length $l=1.27$ mm.

Figure 31 presents the modified flow factor Φ_M for the three test seals at the maximum operating conditions (rotor speed of 3 krpm and air inlet temperature of 300°C). Note the logarithmic scale for Φ_M . The conventional brush seal exhibits a modified flow factor that is approximately 10% of that for the labyrinth seal. At pressure ratios above 2.0, the HBS exhibits approximately 61% of the flow factor of the brush seal, and 7% of that of the labyrinth seal. Hence, the test data evidences the better leakage performance of the HBS against the conventional brush seal and a three-teeth labyrinth seal.

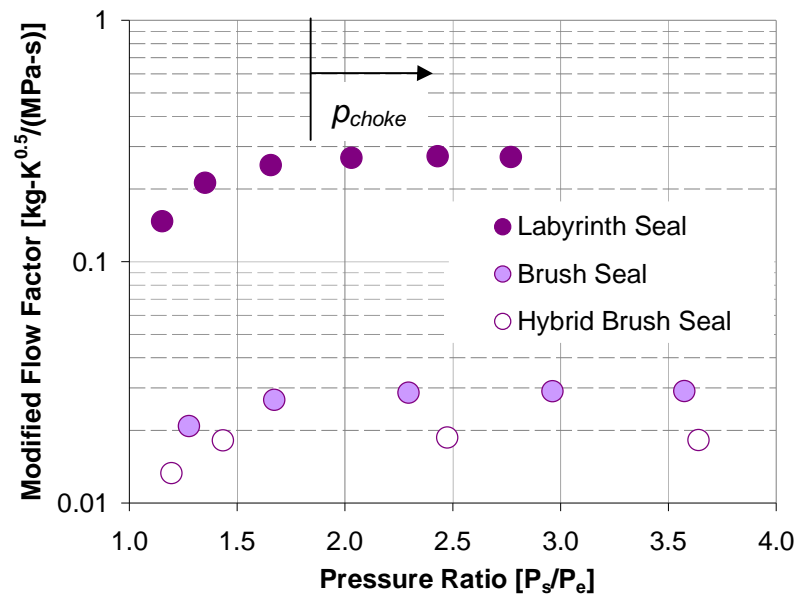


Figure 31: Modified flow factor Φ_M for three seal types versus pressure ratio $[P_s/P_e]$. Air inlet temperature at 300°C. Rotor speed at 3,000 RPM.

Baker [22] presents measurements of leakage in a HBS installed with a diametral interference of 0.70 mm. The current test HBS has a diametral clearance of 0.52 mm. The difference in clearance results in a significant increase in mass flow rate with the current test seal. Figure 32 presents the mass flow rate versus pressure ratio for the previous seal [22] and the current test HBS, while operating at ambient air temperature (30°C) at rotor speeds of 600 RPM and 1,000 RPM, respectively. The current test HBS shows 2 to 2.5 times larger mass flow rate than the previously tested HBS. However, as noted, the current HBS does not contact the disc during unpressurized conditions.

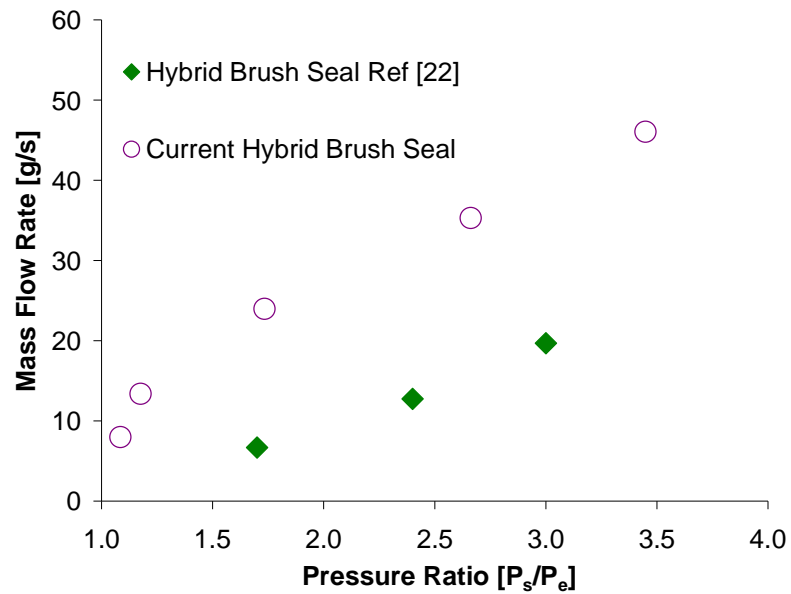


Figure 32: Mass flow rate versus pressure ratio [P_s/P_e] for current HBS and previous HBS (Ref [22]). Air inlet temperature at 30°C. Rotor speed at 1,000 RPM and 600 RPM for the current HBS and previous HBS, respectively.

CHAPTER IX

SEALS DRAG TORQUE AT AMBIENT TEMPERATURE

Performance characteristics other than leakage are also critical to the overall performance of turbomachinery. It is desirable for a seal to provide a large resistance to axial flow while maintaining low levels of rotational drag and avoiding sustained wear over wide ranges of operating conditions. The drag torque multiplied by the rotation speed equals the seal power loss.

Experimental Procedure

A direct current (DC) supply source powers the motor that drives the shaft-disc assembly. The motor maximum speed is 3,500 RPM, drawing up to 9.3 A. For operation at steady state conditions (i.e., constant rotor speed and air inlet temperature), the product of voltage (V) and DC current (i) gives the electrical power ($\dot{\mathcal{P}}$) into the drive motor and delivered to the rotating system. A voltmeter and an ammeter measure the voltage and current, respectively, into the motor at a steady state conditions. Five separate measurements of electrical power at each condition ensure repeatability of the measurement. Assuming electrical power equals the mechanical power, then the drag torque (T_{orque}) of the whole test system is estimated as $T_{orque} = \dot{\mathcal{P}} / \omega$, where ω is the rotor angular speed. Measurements of motor power follow for shaft speeds from 250 rpm to 2.5 krpm (surface speed ~ 22 m/s), at 250 rpm increments.

The procedure assumes that the conversion of electrical energy to mechanical energy is 100% efficient. Under this idealization, no energy is lost to dissipated heat. Since the objective is to compare the magnitude of torque between the test seals, the current experimental method allows for a general relationship to be made as to which sealing methods produce the highest drag torques. Furthermore, San Andrés et al. [6] use the

same procedure to measure the drag torque in a HBS and shoed brush seal (SBS). Comparisons of the torque can therefore be made to the other seals as well.

Results and Discussion

The baseline torque is the torque due to the shaft and the drag due to the roller bearings. Figure 33 shows the derived baseline electrical motor power = $V \times i$, assuming ideal energy conversion, equal to the mechanical power = $Torque \times \omega$ (angular speed). The experimentally determined motor constant is the slope of the voltage versus angular speed, calculated at $k_{V\omega} = V/\omega = 0.24$ V-s/rad. Figure 34 shows the motor voltage and derived drag torque for the baseline case. The torque remains constant for the various angular speeds while the supply voltage to the motor increases as expected.

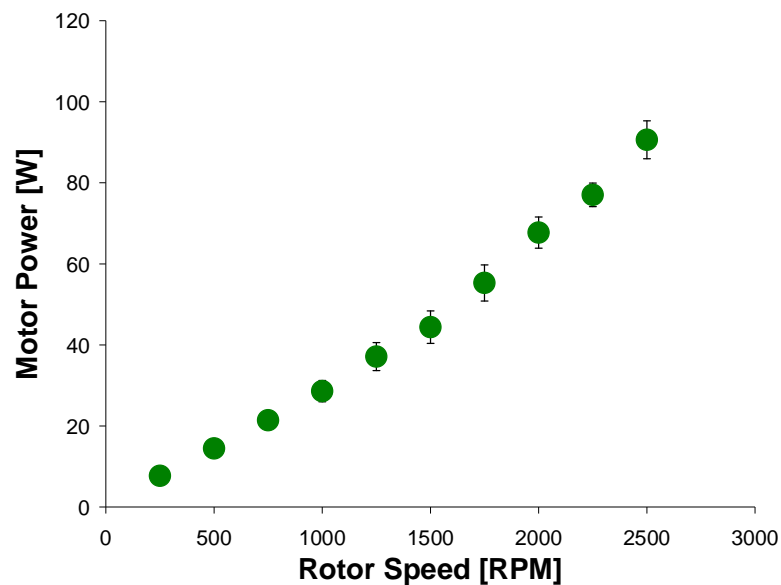


Figure 33: Baseline motor power versus rotor speed. No gas pressurization. Ambient temperature. No seal in place.

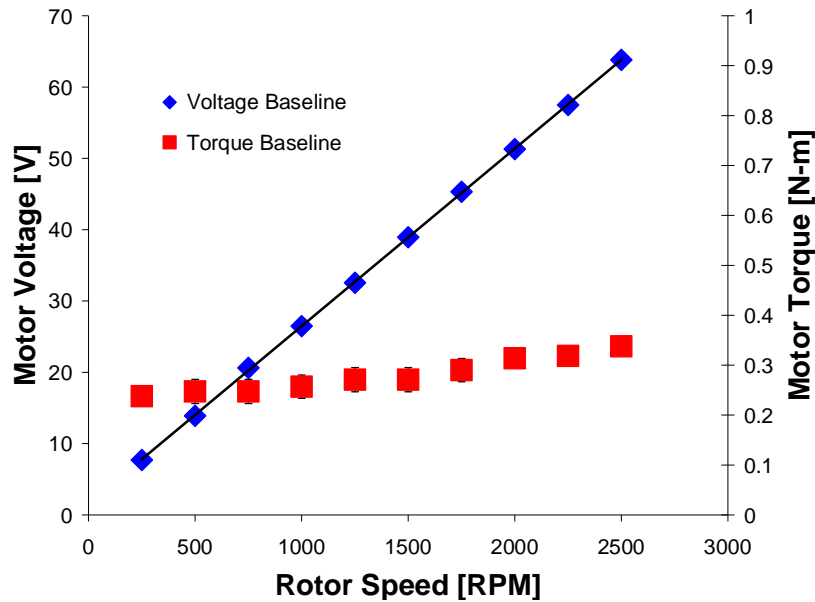


Figure 34: Baseline motor voltage and drag torque versus rotor speed. No gas pressurization. Ambient temperature. Motor speed constant $k_{V\omega} = V/\omega = 0.24$ V-s/rad (0.025 V/rpm).

Figure 35 displays the estimated motor torque versus rotor speed for the three test seals (labyrinth seal, brush seal, and HBS). The measurements correspond to tests conditions with no gas pressurization (i.e. no leakage) and with air supplied at an inlet pressure of 2 bar (absolute). The baseline case represents the torque due to the motor and the rotor alone, without a seal in place. The torque measurements have an average uncertainty of 5.3%.

The motor drive torque without gas through flow (no pressurization) is similar for the three seals, varying little with rotor speed. For operation with a pressure differential (2 bar supply pressure), the HBS induces the largest drag torque, even though it has an initial cold clearance (0.26 mm radial) similar to that of the conventional brush seal. The labyrinth seal has little torque, while the brush seal shows a slightly larger magnitude. The measurement results imply that under a pressurized condition, the HBS experiences more blow-down towards the disc, thus reducing its operating clearance. This also implies a significant reduction in leakage. Appendix E presents measurements of the

surface roughness of the two discs used for testing. The measurements evidence greater blow-down with the HBS.

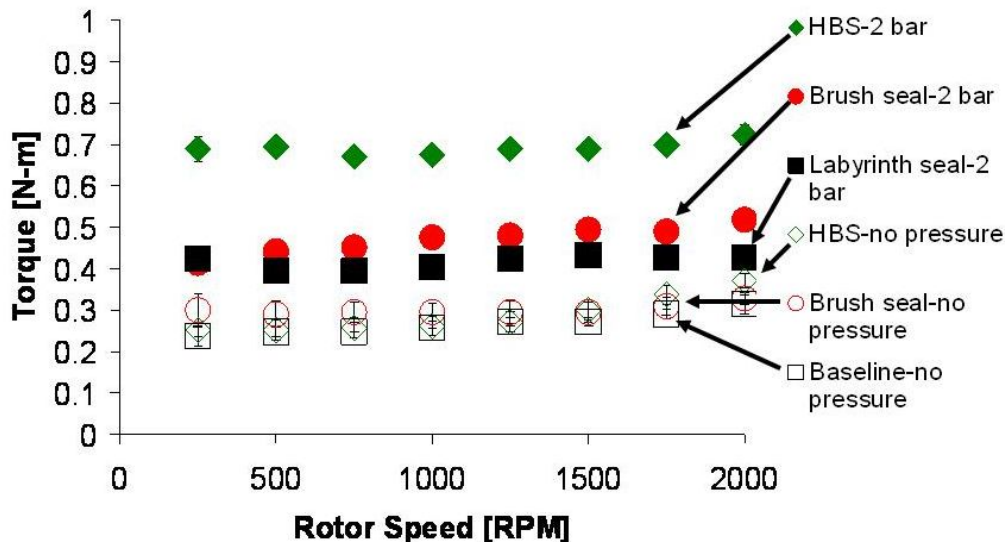


Figure 35: Motor torque versus rotor speed for three seals with supply pressure of 2 bar. Tests without pressures (no leakage) also shown. Operation at ambient temperature (25°C).

Figure 36 depicts the estimated HBS drag torque versus rotor speed. The seal torque equals the motor torque, depicted in Figure 35, less the baseline torque. The figure also includes the estimated measured torque for a HBS operating with an initial interference fit of 0.35 mm [6]. The current HBS, on the other hand, has a nominal radial clearance of 0.26 mm (without pressurization and at room temperature). Hence, the current test HBS shows much less torque, particularly for operation without gas through flow.

In the previous HBS test configuration, after pressurization, the resilient pads lift-off due to a hydrostatic effect even without rotor spinning; hence, the seal torque drastically decreased by $\sim 1/10$, as seen in Figure 36 (compare results with no pressure and feed pressure at 1.7 bar). When designed to operate with an initial clearance, the current HBS has a similar torque at the pressure condition of 2 bar.

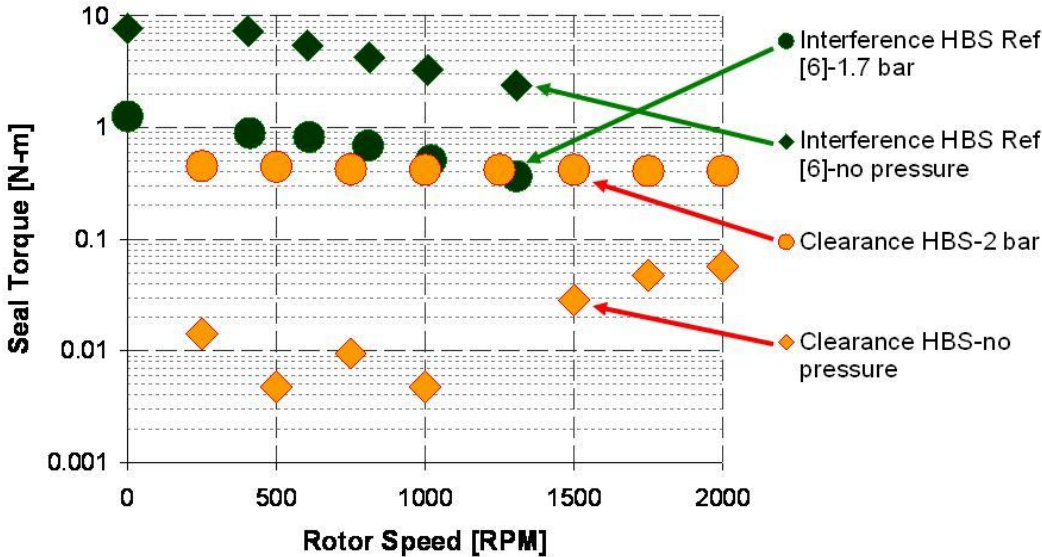


Figure 36: Torque versus rotor speed for current HBS and other HBS operating at inlet pressure up to 2.0 bar and 1.7 bar, respectively. Operation at ambient temperature (25°C).

CHAPTER X

IDENTIFICATION OF SEAL EQUIVALENT MECHANICAL PARAMETERS FROM IMPACT LOAD TESTS

This section details the identification of the seals equivalent mechanical parameters from impact load tests. The bristles in brush seals can provide stiffness and damping to the test system. Friction occurs between the bristles (interbristle contact), the bristles and the disc, and the bristles and the backing plate. The bristle material, backing plate material, disc material, and severity of contact affect the frictional forces that develop within a particular brush seal. Dry friction and material structural loss factor determine the damping in the brush seal. The HBS includes bristle elements and pads, and therefore adds stiffness and damping.

Experimental Procedure

Impact load measurements on the test rotor-disc characterize the rotor fundamental modal parameters, stiffness (K_{eq}) and mass (M_{eq}), and its elastic natural frequency, $\omega_n = (K_{eq}/M_{eq})^{1/2}$. Measurements with and without the test seal (brush seal or hybrid brush seal) at increasing supply pressures and no shaft rotation allow for the seal mechanical parameters to be extracted.

A pair of cylindrical roller bearings rigidly supports the shaft. The steel shaft ($E=200$ GPa, $\rho=7850$ kg/m³) has length $L=275$ mm and radius $r=6.36$ mm, cross sectional area $A=\pi r^2=127$ mm², and area moment of inertia $I=1270$ mm⁴. The disc of mass $M_{disc}=3.55$ kg and a test seal are located at $L_s=210$ mm away from the bearing supports. The location for measurement of rotor displacements with the optical sensor and impact load application is $L_e=235$ mm. Figure 37 depicts the predicted first elastic mode shape for the shaft-disc and seal assembly. Note that the ball bearing stiffnesses are high enough to

clamp the rotor on its drive end side. Hence, the fundamental mode shape resembles that of a cantilever beam.

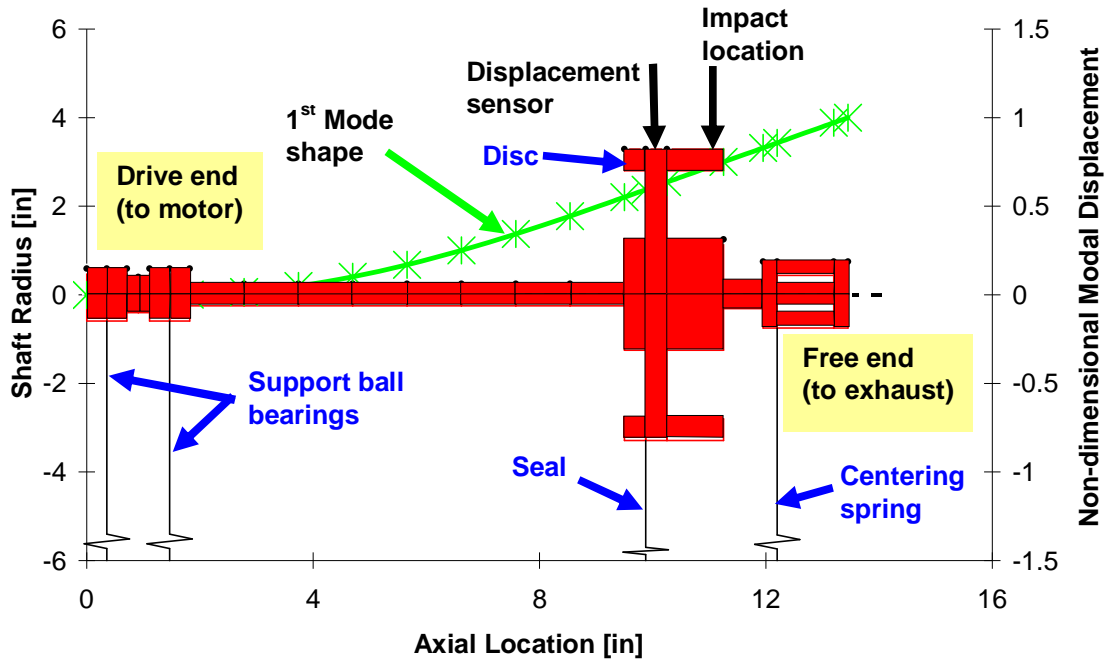


Figure 37: First mode shape of test rotor and element model with structural and support elements.

Figure 38 presents the schematic view of the shaft-disc and seal assembly and its representation as an equivalent single degree of freedom mechanical system model. The fundamental deflection shape for a cantilever beam is

$$\psi(z) = \frac{(3Lz^2 - z^3)}{2L^3} \quad ; \quad 0 < z < L \quad (12)$$

Kinetic and strain energy balances render the test system equivalent stiffness (K_{eq}) and mass (M_{eq}) as

$$K_{eq} = \frac{3EI}{L^3} \left(\frac{1}{\psi(L_e)} \right)^2 + K_s \left(\frac{\psi(L_s)}{\psi(L_e)} \right)^2 \quad (13)$$

$$M_{eq} = \left(\int_0^L \rho A \psi(z)^2 dz \right) \left(\frac{1}{\psi(L_e)} \right)^2 + M_{disc} \left(\frac{\psi(L_s)}{\psi(L_e)} \right)^2 \quad (14)$$

Without a seal in place ($K_s=0$), the system equivalent stiffness and mass are $K_{shaft(e)} = 60.5$ N/mm and $M_{eq}=3.04$ kg, respectively. With these values, the predicted system natural frequency $\omega_n = 22.4$ Hz which agrees well with the measured frequency at 21.2 Hz.

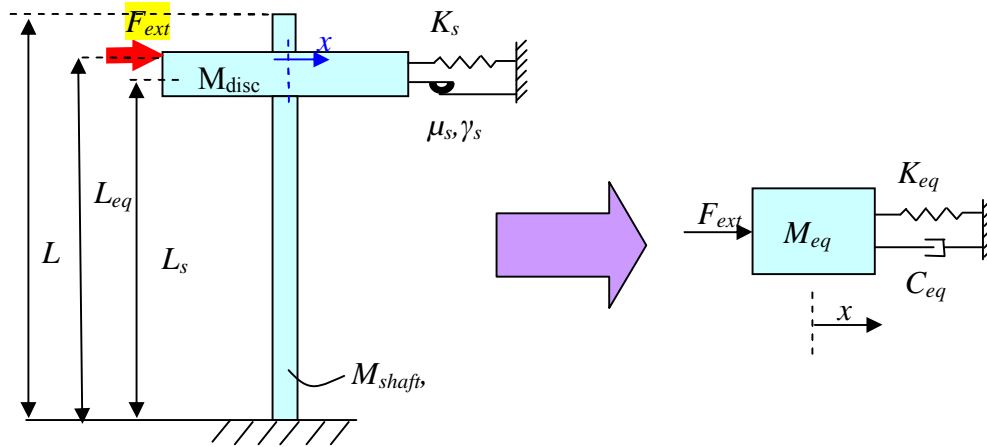


Figure 38: Schematic view of shaft-disc and seal assembly and its equivalent representation as a single degree of freedom mechanical system.

The rotor-disc and seal assembly is typically modeled as an equivalent single degree of freedom system with viscous damping, i.e.

$$M_{eq} \ddot{x} + C_{eq} \dot{x} + K_{eq} x(t) = F(t) \quad (15)$$

Above, $F(t)$ and $x(t)$ are the (input) impact load and ensuing rotor displacement, respectively. The inertia, viscous damping, and stiffness coefficients (M_{eq} , C_{eq} , K_{eq}) are equivalent parameters at the location of measurement. In the frequency domain, let

$$x = \bar{X} e^{i\omega t}, \quad F = \bar{F} e^{i\omega t} \quad (16)$$

which assumes the system is linear. Substitution of Eq. (13) into Eq. (12) gives the algebraic equation

$$\left[(K_{eq} - \omega^2 M_{eq}) + i \omega C_{eq} \right] \bar{X} = \bar{F} \quad (17)$$

The flexibility function is defined as

$$\frac{\bar{X}}{\bar{F}} = \frac{1}{\left[(K_{eq} - \omega^2 M_{eq}) + i \omega C_{eq} \right]} \quad (18)$$

Delgado and San Andrés [21] emphasize that a viscous damping type characterization in seals with bristles is (obviously) rather poor. Physical reasoning determines that the mechanical energy dissipation in a brush seal is due to structural or material damping (γ) and dry-friction (μ) or Coulomb-type mechanisms. The relationship between these mechanisms is [21]

$$C_{eq} = \frac{\gamma_{eq} K_{eq}}{\omega} + \frac{4\mu |\bar{F}|}{\pi\omega |\bar{X}|} \quad (19)$$

where $|F/$ and $|X|$ are the amplitude of the applied force and displacement at a certain frequency. Note that the viscous damping coefficient is nonlinear, inversely proportional to the amplitude of motion $|X|$ and excitation frequency ω . Algebraic manipulation of Eq. (19) leads to the flexibility function as [21]

$$\frac{|\bar{X}|}{|\bar{F}|} = \frac{1}{K_{eq}} \left(\frac{-(\lambda \gamma_{eq}) + \sqrt{(1 - \lambda^2)(1 - r^2)^2 + \gamma_{eq}^2}}{(1 - r^2)^2 + \gamma_{eq}^2} \right) \quad (20)$$

where $\lambda = 4\mu/\pi$ and r is the frequency ratio ω/ω_n .

A computational code imports the measured flexibility function for the various test cases and using a built-in nonlinear root solver function finds the parameters that best approximate the measured data using the flexibility model in Eq. (20). The curve fit outputs the specified variables i.e., equivalent stiffness (K_{eq}), natural frequency (ω_n), structural loss coefficient (γ), and dry friction coefficient (μ). Incidentally, the program performs the same procedure for a viscous damping model and gives the damping ratio

($\zeta = \frac{C_{eq}}{2\sqrt{K_{eq}M_{eq}}}$). The program also outputs the goodness of fit, or correlation value,

between each of the models and the measured flexibility, thus evidencing which model is more physically accurate.

Results and Discussion

Figure 39 displays the flexibility function (\bar{X}/F) versus excitation frequency for tests conducted with the hybrid brush seal in place at absolute inlet pressures of 1.0, 1.5, and 2.0 bar. Results include the baseline condition (no seal) and a test with the seal in place and no air flow (pressure ratio=1.0). The log scale for the vertical axis highlights the magnitude of the peak amplitudes. The HBS peak amplitude is lower by a factor of ~10 or more implying much larger damping to the system. Figure 40 presents the flexibility for the test system with the brush seal in place. The test conditions (temperature and supply pressure) are identical to those conditions for the HBS. At the natural frequency, the maximum flexibility of the brush seal is noticeably higher than that of the HBS, thus indicating less damping.

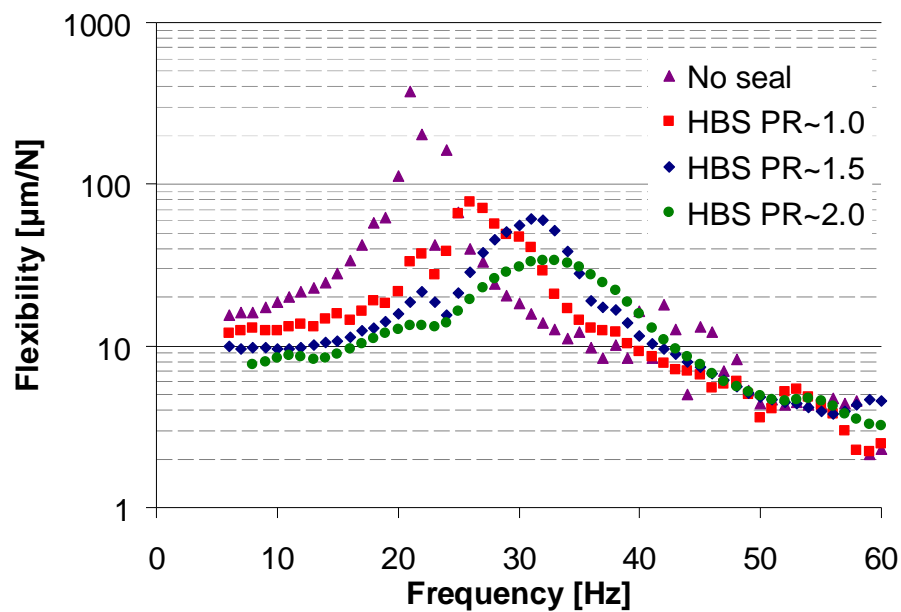


Figure 39: Amplitude of flexibility function for test rotor and hybrid brush seal (HBS). Tests with air at supply pressure/exhaust pressure (PR)=1.5 and 2.0. Baseline (no seal) and with seal and no pressurization (PR=1.0) included. Impact load tests. No shaft rotation. Ambient temperature=25°C

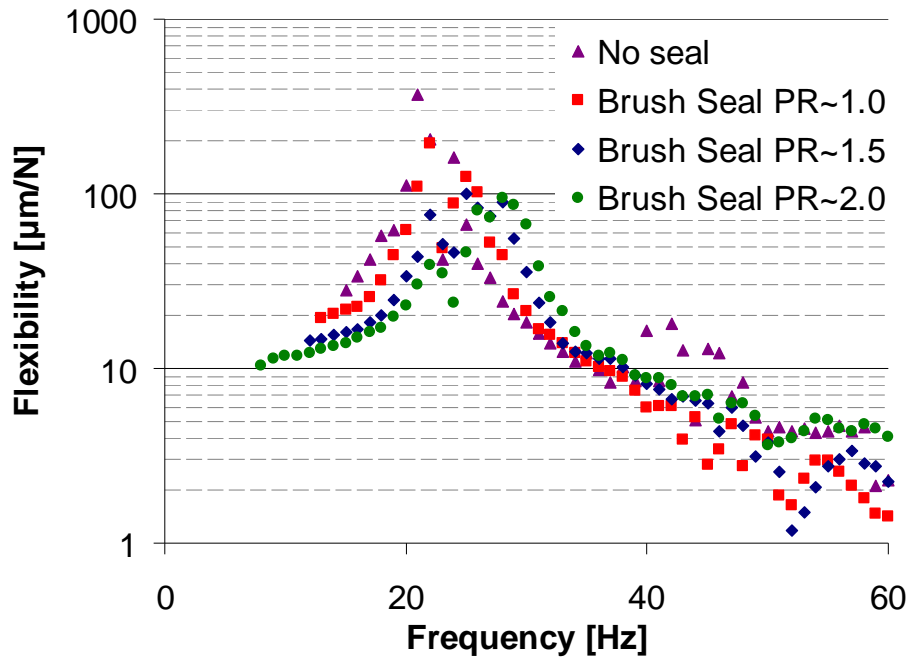


Figure 40: Amplitude of flexibility function for test rotor and brush seal. Tests with air at supply pressure/exhaust pressure (PR)=1.5 and 2.0. Baseline (no seal) and with seal and no pressurization (PR=1.0) included. Impact load tests. No shaft rotation. Ambient temperature=25°C

The structural damping-dry friction (γ , μ) energy dissipation model shows a better goodness of fit for all cases with a seal in place. Table 6 presents the system coefficients for the cases with the HBS and brush seal for increasing supply pressures as well as the correlation value between the measured flexibility and the model curve fit. Notice the HBS has a consistently higher structural damping than the brush seal. Also, the structural (γ) damping and dry friction (μ) coefficients tend to increase at higher supply pressures.

For a HBS, Delgado and San Andrés [21] estimate a similar dry friction coefficient, $\mu=0.55$, and a material loss factor, $\gamma=0.25$, at unpressurized conditions ($P_R=1$). It is also important to note that the natural frequency and system equivalent stiffness increase as the supply pressure increases. Test seal stiffness is easily derived from Eq. (12) as

$$K_s = \left(K_{eq} - K_{eq(no\ seal)} \right) \left(\frac{\psi(L_e)}{\psi(L_s)} \right)^2 \quad (21)$$

Table 6 reports the extracted seal stiffness (K_s) increasing with supply pressure. This is likely due to the bristles and pads blowing-down to contact the disc. The HBS has ~25% more stiffness than the conventional brush seal. Most importantly, both seals introduce very large amounts of damping when compared to the labyrinth seal.

The identification analysis shows that the correlation coefficients (goodness of fit) have an average correlation value of 0.94 between the measured flexibility and the generated curve fit using the structural damping-dry friction model.

Table 6: Equivalent system coefficients with HBS and brush seal at three supply pressures. Air inlet at 25°C. No shaft rotation.
(P_R =supply pressure/exhaust pressure).

	HBS			Brush Seal			No Seal
	P_R =1	P_R ~1.5	P_R ~2.0	P_R =1	P_R ~1.5	P_R ~2.0	P_R =1.0
Dry friction, μ	0.13	0.41	0.56	0.70	0.68	0.46	
Structural loss factor, γ	0.18	0.21	0.38	~0	0.28	0.17	
Natural frequency, ω_n [Hz]	26.7	30.8	32.6	21.3	25.9	28.0	21.2
Mass, M_{eq} [kg]	3.1	3.0	3.1	3.3	3.4	3.3	3.2
Stiffness, K_{eq} [N/mm]	88	113	133	59	92	104	57
Test Seal Stiffness, K_s [N/mm]	45	81	110	2.9	51	68	
R^2 (correlation factor)	0.96	0.99	0.99	0.81	0.94	0.94	0.93

Analytical w/o seal in place: $K_{eq} = 60.5$ N/mm and $M_{eq} = 3.04$ kg, $\omega_n = 22.4$ Hz

Figure 41 and Figure 42 show the experimental and physical model flexibility functions versus frequency for the HBS and conventional brush seal, respectively. The physical model with structural damping-dry friction energy dissipation characteristics reproduces best the test data. For tests with supply pressure at 2.0 bar, the model with viscous damping shows a damping ratio $\zeta = 0.11$ for the HBS, and $\zeta = 0.05$ for the conventional brush seal. Hence, the HBS offers substantially more viscous damping than the conventional brush seal.

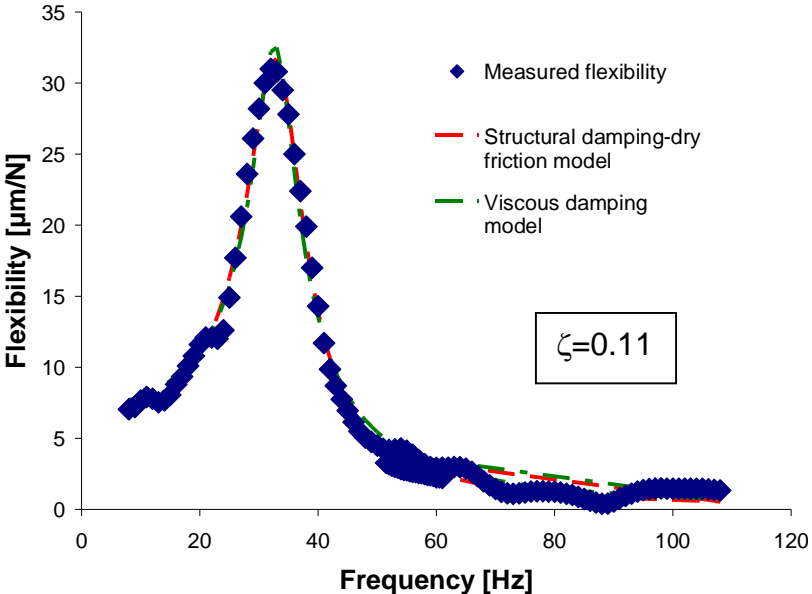


Figure 41: Measured flexibility in HBS and physical models with (a) structural damping-dry friction and (b) viscous damping. Supply pressure ~ 2.0 bar. Ambient temperature, no shaft rotation

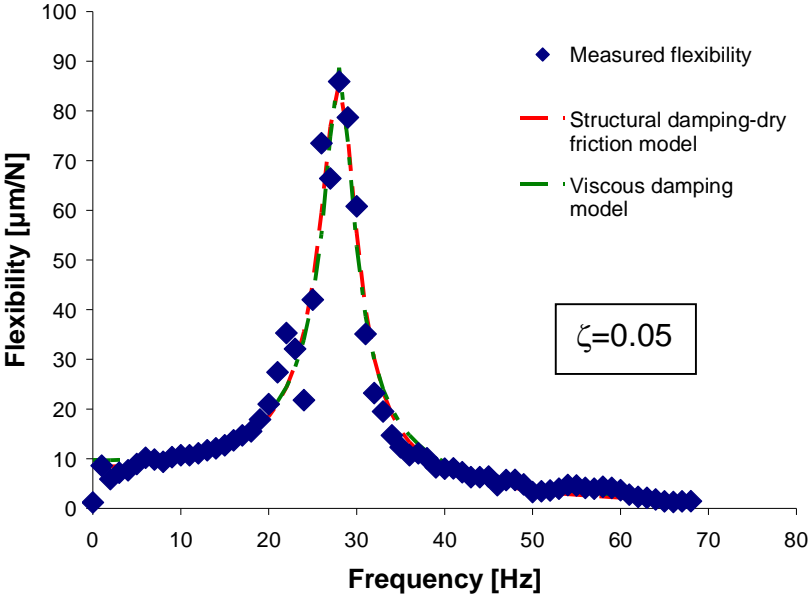


Figure 42: Measured flexibility in brush seal and physical models with (a) structural damping-dry friction and (b) viscous damping. Supply pressure ~ 2.0 bar. Ambient temperature, no shaft rotation.

For completeness and comparison with measurements obtained with the brush seal and HBS, Figure 43 depicts the flexibility function for the test condition without a seal in place. The viscous model gives a very small damping ratio, $\zeta = 0.016$. Hence, both seals introduce significant damping into the vibratory system.

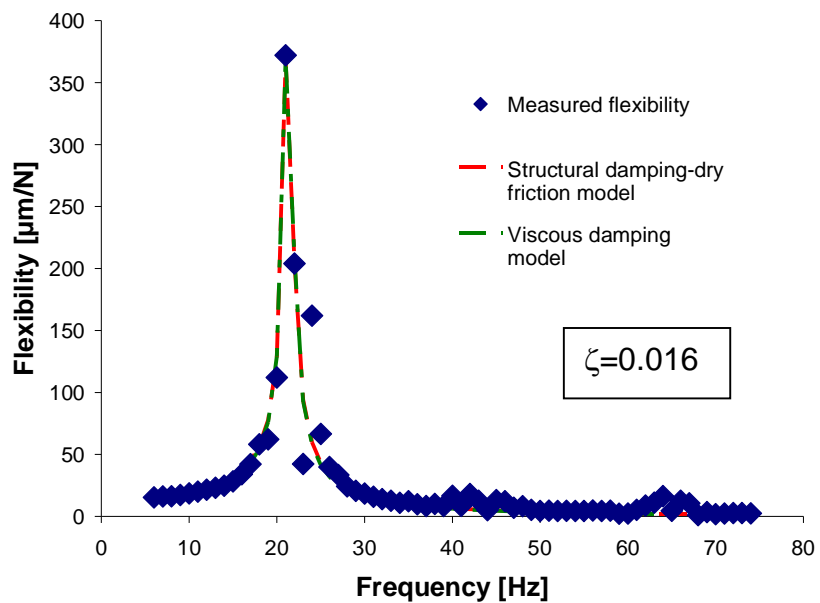


Figure 43: Measured flexibility of test system without a seal in place and physical models with (a) structural damping-dry friction and (b) viscous damping. Ambient temperature, no shaft rotation, no pressurization.

CHAPTER XI

CONCLUSIONS AND RECOMMENDATIONS

Improvements in sealing technology aid to increase efficiency by reducing leakage and wear in rotating machinery. By operating at a constant clearance, the labyrinth seal offers low drag torque to the system but suffers from relatively poor flow resistance. The benefit of brush seals in reducing leakage has been demonstrated for aero and industrial gas turbines. The Hybrid Brush Seal (HBS) represents a novel advance to further decrease leakage and wear by more carefully regulating the operating clearance. The presence of a hydrodynamic film prevents the wear inevitable in a conventional brush seal. The HBS offers the additional benefit of high axial stiffness. This means that the HBS can operate at higher pressure differentials that the brush seal cannot due to the brush seals inherently low axial stiffness.

A high temperature test rig is constructed to quantify the leakage performance of annular seals. Three seals are tested: a labyrinth seal, a brush seal and a HBS. Hot pressurized air is supplied to an air pressurization cylinder. Within the cylinder is a shaft with a disc located on one end. The disc is located within the test seal with the exhaust air passing into a duct for removal. The opposing end of the shaft is supported by two roller bearings with a connected quill shaft passing to the drive motor. The rig is instrumented to measure flow rate, pressures, temperatures, rotor speed, and the location of the disc within the seal.

Measurements of mass flow rate for the labyrinth seal, brush seal, and HBS are obtained at a range of temperatures (30°C-300°C), supply pressures (1-3.5 bar), and rotor speeds (0 RPM-3,000 RPM). The flow factor is used to compare the performance of the seals at various supply pressures and temperatures. The flow factor shows little dependence on temperature for all three test seals and a slight dependence on the supply pressure after choked conditions ($P_s > 1.89$ bar). Further, no change is noted in the flow rate due to rotor speed for the limited surface speeds (27m/s). The HBS offers significant

decrease in the flow rate compared to a similarly sized labyrinth seal, approximately 38% of the leakage. Further, the HBS has a flow rate ~61% that of a conventional brush seal, even though both seals have nearly identical diametrical clearances, 0.52 mm, at room temperature and prior to air pressurization. The reduction in flow factor (lesser leakage) is likely due to the HBS experiencing a greater degree of blow-down than the brush seal.

Clearance measurements for the labyrinth seal show nearly constant clearance at temperatures to 300°C, which closely matches the modeled clearance change. The measured clearances are used to predict the flow rate through the three-teeth labyrinth seal using an iterative model based upon flow past a single tooth. The predictions closely match the measured flow rate at supply pressures less than 1.7 bar. However, the predictions overpredict by approximately 25% at larger supply pressures. A porous medium fluid flow model predicts the leakage for the brush seal and HBS. The model uses an effective thickness parameter. The model severely underpredicts the flow at low supply pressures when the seals have large clearances that do not fit well the porous medium model.

Torque measurements of the motor with the test seals in place evidence differing levels of drag induced by each seal. The HBS experiences the largest drag torque at a supply pressure of 2.0 bar. This indicates a greater degree of blow-down at pressurization than the brush seal as both seals have the same clearance at unpressurized conditions.

Impact load tests with the brush seal and HBS render the system flexibility in the frequency domain. The system is modeled as a single degree of freedom system. Without any test seal in place, predictions of the system natural frequency, mass, and stiffness match well the measured values. Impact load tests with the brush seal and HBS show increases in the equivalent stiffness and viscous damping at higher supply pressures for both. A curve fit of the measured flexibility function gives the dry friction and structural loss factor damping using an energy dissipation model. In terms of

damping ratio, the HBS has twice the damping as the brush seal at the maximum test supply pressure of 2.0 bar.

Planned dynamic load tests with the test seals will determine their rotordynamic force coefficients and influence on the stability and critical speeds of the rotating system. To further validate the HBS technology, it is recommended to perform measurements of flow rate and drag torque at even higher temperatures (600°C) and surface speeds (100 m/s) to replicate conditions typical in a power gas turbine section.

Future plans also include measurements and predictions of flow rate in other seal types. Of particular interest, the Hydrostatic Advanced LO-leakage (HALO™) seal represents the next generation following the HBS. The HALO™ seal dispenses with the bristle matrix but retains the resilient pad elements. The seal begins operation at a large positive clearance with respect to the rotor. As the supply pressure increases the pads on the seal are drawn inward, thus drastically decreasing the clearance. Flow rate measurements of this novel technology will quantify the level of leakage reduction.

REFERENCES

- [1] Chupp, R. E., Hendricks, R. C., Lattime, S. B., and Steinetz, B. M., 2006, "Sealing in Turbomachinery", *AIAA J. of Prop. Power*, **22**(2) pp.313-349.
- [2] Floyd, C. G., 1986, "Gas Seals for Rotating Shafts", *Tribology International*, **19**(4) pp.204-211.
- [3] Ferguson, J. G., 1988, "Brushes as High Performance Gas Turbine Seals," ASME Paper No. 88-GT-182.
- [4] Chupp, R. E., Johnson, R. P., and Loewenthal, R. G., 1995, "Brush Seal Development for Large Industrial Gas Turbines", AIAA Paper No.1995-3146.
- [5] Justak, J. F., and Crudginton, P. F., 2006, "Evaluation of a Film Riding Hybrid Seal," AIAA Paper No. 2006-4932.
- [6] San Andrés, L., Baker, J., and Delgado, A., 2009, "Measurements of Leakage and Power Loss in a Hybrid Brush Seal", *ASME J. Eng. Gas Turbines Power*, **131**(1), pp.012505-1-6.
- [7] Childs, D. W., 1993, *Turbomachinery Rotordynamics: Phenomena, Modeling and Analysis*, John Wiley & Sons, New York, Chapter 5.
- [8] El-Gamal, H. A., Awad, T. H., and Saber, E. 1996, "Leakage from Labyrinth Seals Under Stationary and Rotating Conditions", *Tribology International*, **29**(4) pp.291-297.
- [9] Alford, J. S., 1975, "Nature, Causes, and Prevention of Labyrinth Air Seal Failures", *AIAA J. of Aircraft*, **12**(4), pp.313-318.
- [10] Childs, D., Baskharone, E., and Ramsey, C., 2006, "Test Results for Rotordynamic Coefficients of the SSME HPOTP Turbine Interstage Seal with Two Swirl Brakes", *ASME J. Tribol.*, **113**(3) pp.577-583.
- [11] Denecke, J., Färber, J., Dullenkopf, K., and Bauer, H.-J., 2008, "Interdependence of Discharge Behavior, Swirl Development and Total Temperature Increase in Rotating Labyrinth Seals", ASME Paper No. GT2008-51429.
- [12] Choi, D. C., Rhode, D. L., and Mirzamoghadam, A., 2004, "Labyrinth Seal Design Changes to Reduce Rim Seal Coolant" AIAA Paper No. 2004-3572.

- [13] Crudgington, P. F, and Bowher, A., 2003, “Brush Seal Blow Down”, AIAA Paper No. 2003-4697.
- [14] Franceschini, G., Jones, T. V., and Gillespie, D. R. H., 2008, “Improved Understanding of Blow-Down in Filament Seals”, ASME Paper No. GT2008-51197.
- [15] Conner, K. J., and Childs, D. W., 1993, “Rotordynamic Coefficient Test Results for a Four-Stage Brush Seal”, AIAA J. of Prop. Power, **9**(3), pp.462-465.
- [16] Basu, P., Datta, A., Loewenthal, R., Short, J., and Johnson, R., 1994, “Hysteresis and Bristle Stiffening Effects in Brush Seals”, AIAA J. of Prop. Power, **10**(4) pp. 569-575.
- [17] Zhao, H., and Stango, R. J., 2007, “Role of Distributed Interbristle Friction Force on Brush Seal Hysteresis”, ASME J. Tribol., **129**(1) pp.199-204.
- [18] Dinc, S., Demiroglu, M., Turnquist, N., Mortzheim, J., Goetze, G., et al., 2006, “Fundamental Design Issues of Brush Seals for Industrial Applications”, ASME J. Turbomach., **124**(2) pp.293-300.
- [19] Aksit, M. F., 2003, “Analysis of Brush Seal Bristle Stresses with Pressure-Friction Coupling”, ASME Paper No. GT2003-38718.
- [20] Delgado, A., San Andrés, L., and Justak, J. F., 2004, “Analysis of Performance and Rotordynamic Force Coefficients of Brush Seals with Reverse Rotation Ability”, ASME Paper No. GT2004-53614.
- [21] Delgado, A., and San Andrés, L., 2007, “Identification of Structural Stiffness and Damping Coefficients of a Shoed Brush Seal,” ASME J. of Vib. Acoust., **129**(5), pp.648-655.
- [22] Baker, J., 2008, “Measurements of Leakage, Power Loss and Rotordynamic Force Coefficients in a Hybrid Brush Seal”, Master’s Thesis, Texas A&M University, College Station.
- [23] Delgado, I. R., and Proctor, M. P., 2006, “Continued Investigation of Leakage Power Loss Test Results for Competing Turbine Engine Seals”, AIAA Paper No. 2006-4754.
- [24] Chupp, R. E., and Holle, G. F., 1996, “Generalizing Circular Brush Seal Leakage through a Randomly Distributed Bristle Bed”, ASME J. of Turbomach., **118**(1), pp.153-161.

- [25] San Andrés, L., 2003, “Analysis of Performance and Rotordynamic Force Coefficients of Brush Seals with Reverse Rotation Ability”, Final Report to Advanced Turbomachinery Solutions (ATS), March.
- [26] Wood, P. E., Jones, T. V., 1999, “Test Facility for the Measurement of Torques at the Shaft to Seal Interface in Brush Seals”, ASME J. of Eng. Gas Turbines Power, **121**(1), pp.160-166.

APPENDIX A

CALIBRATION OF FLOW METER FOR OPERATION AT A RANGE OF PRESSURES AND TEMPERATURES

Mass flow measurements occur over a range of temperatures and pressures. A turbine flow meter measures the volumetric flow rate upstream of the heater. Based upon conservation of mass, the mass flow rate through the piping at the upstream location is equal to the mass flow rate through the seal. The turbine flow meter outputs a frequency spectrum signal in which the peak frequency corresponds to the volumetric flow rate past the flow meter in actual cubic feet per minute (ACFM). The manufacturer of the turbine flow meter only provides calibration data for the flow meter in standard cubic feet per minute (SCFM) for air at a pressure of 1 bar (14 psia) and temperature of 16°C when the flow meter is operating at conditions of 7.9 bar (100 psig) and 23 °C.

The measurement procedure for the leakage uses an electromechanical valve to vary the pressure in the air pressurization chamber. As the valve opens to increase the pressure in the air pressurization cylinder, the pressure at the flow meter drops below the calibrated value of 100 psig and the calibration is no longer accurate. Therefore, it is best to transform the manufacturer's calibration from SCFM to ACFM using

$$ACFM = SCFM * \frac{P_{std} T_{cal}}{P_{cal} T_{std}} \quad (A1)$$

where the pressure and temperature are expressed in absolute values for the calibrated and standard values. Table A1 presents the calibration data using SCFM and ACFM with the flow meter frequency.

Table A1: Calibration data in SCFM and ACFM at specific frequencies

Flow meter frequency [Hz]	Volumetric flow rate [SCFM]	Volumetric flow rate [ACFM]
1286.791	102.7458	13.548521
1081.915	86.3817	11.390678
951.924	77.0461	10.159644
820.234	65.984	8.7009456
709.718	57.5222	7.5851348
627.041	50.9018	6.7121392

543.754	44.3313	5.8457237
465.429	38.1686	5.0330825
402.892	33.1686	4.3737601
350.946	29.2503	3.8570755
300.686	25.1441	3.3156136
263.02	22.2695	2.936556
230.809	19.7965	2.6104551
196.331	17.1628	2.2631636
168.48	15.1377	1.9961249
139.536	13.1444	1.7332794
114.994	11.4752	1.5131712
91.896	10.0258	1.3220469
70.723	8.747	1.1534186
42.896	7.357	0.970127

Once the measurements are complete, the volumetric flow measurements and measured pressure and temperature at the flow meter can be used to find the mass flow rate based upon the ACFM as follows

$$\dot{m} = ACFM * \frac{P_{act}}{P_{std}} \frac{T_{std}}{T_{act}} * \rho_{std} \quad (A2)$$

where ρ is the density of air at standard conditions. This allows for changes in the line pressure and temperature to be accounted for in terms of the volumetric flow rate while maintaining the conservation of mass for the entire system.

APPENDIX B

CALIBRATION OF PRESSURE SENSOR

Two types of pressure transducers are used in the measurements presented: a high temperature sensor and two miniature pressure sensors. The high temperature pressure sensor is located at the hot air inlet leading into the pressurization chamber and represents the supply pressure, P_s . The pressure sensor can accurately measure pressure at temperatures up to the limits for the test conditions, 300°C. No manufacturer calibration is included with the sensor due to the calibration limits being adjustable. Therefore, a static pressure loader is used to determine the voltage output for a range of pressures. Pressure increments of 10 psi are used from 0 psig to 100 psig. This represents the entire range of operation for the high temperature pressure sensor. Figure B1 displays the calibration curve for the high temperature pressure sensor along with the equation for converting from voltage to psig. Calibration can only be done at room temperature, but manufacturer claims no dependence on temperature.

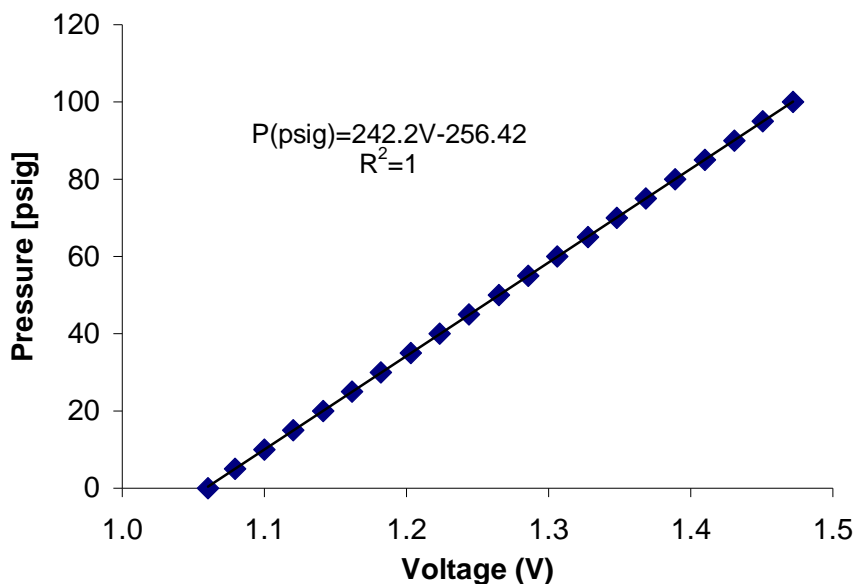


Figure B1: Pressure versus output voltage for high temperature pressure sensor at ambient air temperature for use at supply side of disc. Calibration curve with goodness of fit listed.

Miniature pressure sensors are used at the flow meter, for accurate calculation of the flow rate, and at the exhaust end of the test rig, P_e , to ensure the exit remained close to ambient. The miniature sensors are used due to their low cost, small size, ease of attachment to piping, and regular use in the lab. Due to their previous use in the lab, calibration curves exist for the sensors. However, the sensor sensitivity is strongly dependent on the DC supply voltage to the sensors. For that reason, calibrations are taken at a single supply voltage. This supply voltage is closely monitored during testing to ensure that the sensor sensitivity does not change. Figure B2 present the pressure versus output voltage for the two miniature sensors at a specified supply voltage at room temperature.

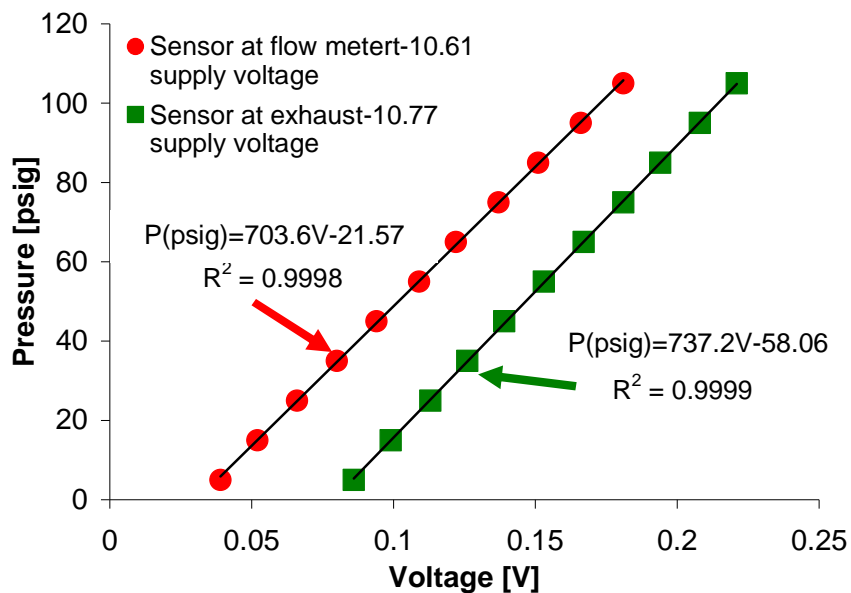


Figure B2: Pressure versus output voltage for miniature pressure sensors at specified supply voltages. Ambient air temperature. Calibration curves with goodness of fit listed.

APPENDIX C

USER INTERFACE FOR DATA ACQUISITION AND CONTROL

A custom data acquisition and control system are designed for use on a Field Programmable Gate Array (FPGA) board. Figure C1 displays the FPGA board with four modules. Each module is responsible for a particular input/output (I/O) function. The board is capable of receiving 12 voltage analog inputs (-10 to 10 V) and 3 thermocouple inputs. Additionally, the board may send up to 3 voltage analog outputs (-10 to 10 V) or 3 current analog outputs (4 to 20 mA).



Figure C1: FPGA board with analog inputs, analog outputs, and thermocouples wired.

The FPGA system works by loading a FPGA Virtual Instrument (VI) onto the board pictured in Figure C1. The FPGA VI controls the I/O, timing, and sampling functions for the data acquisition. A separate host VI is then created to interact with the FPGA VI in order to receive the raw binary signals and convert them into useful voltage units. The core FPGA VI architecture does not typically change, while the host VI can be adapted for the specific uses required. To begin operation of the rig, the host VI connects to the board. Once operating, a tabbed user interface allows for the gauge pressure voltages to be set. The user can then alter the temperature and supply pressure and acquire data for

the flow, temperature, pressures, and disc displacement. All of this information is saved based upon user input. Figure C2 presents two of the tabbed interfaces used for initializing the test rig and for recording the relevant data.

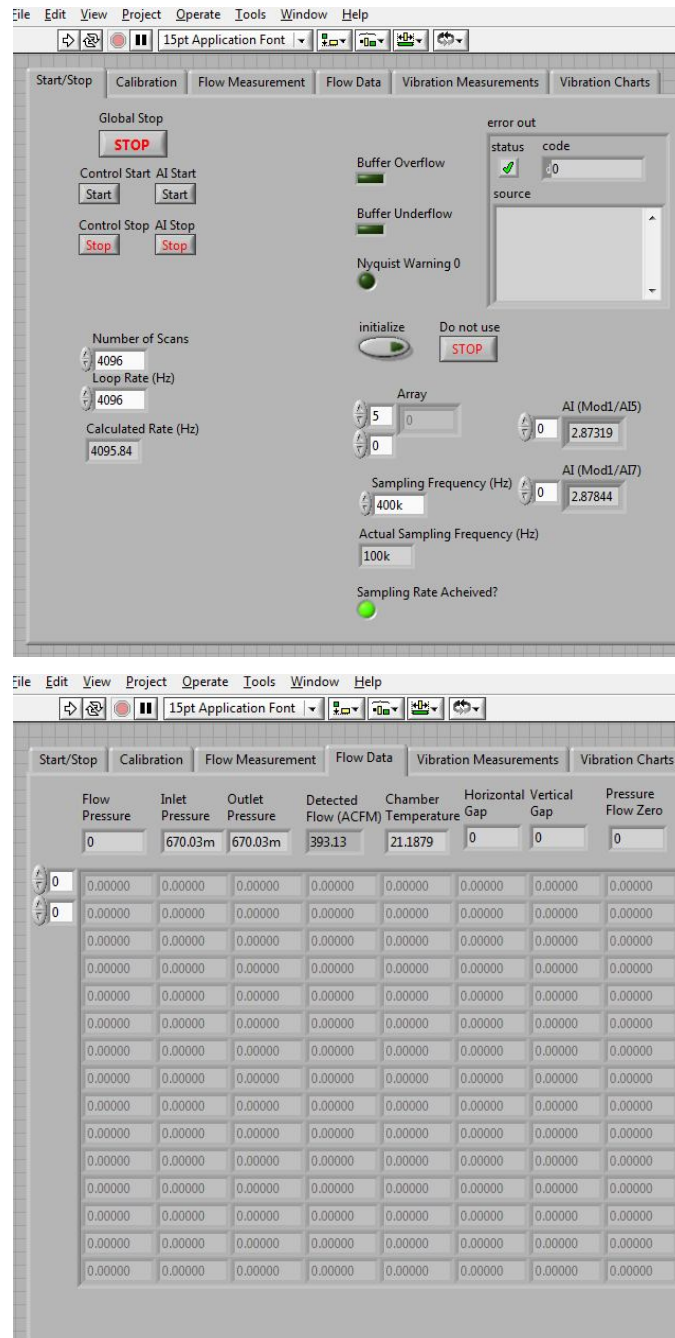


Figure C2: Two example panes used for the tabbed user interface on the host VI for initializing test rig (top) and recording relevant test data (bottom).

APPENDIX D

CALIBRATION OF HIGH TEMPERATURE OPTICAL SENSORS

Previous measurements by Baker [22] include eddy current sensors to center the disc within the seal and measure the motion of the disc during excitation. As the eddy current sensors are not capable of withstanding the high temperature environment, optical sensors are used to measure the location of the disc with the seal. Two optical sensors, serial number 1781 and 1780, measure the vertical and horizontal distance to the disc. The sensors output a voltage nearly proportional to the distance from a target. Since the calibration is different based upon the reflectivity of the target, the sensors are calibrated using the test disc instead of using the provided manufacturer calibrations. To calibrate the sensors, the test disc is secured to a machining lathe with a sensor mounted perpendicular as in the rig. The sensor is then moved closer from a zeroed position on the lathe. The lathe outputs the distance moved from the zeroed position and the corresponding voltage is recorded. Figure D1 presents the distance versus voltage calibration for the two optical sensors from calibration on the lathe. Manufacturer notes that temperature has no influence on the calibration of the sensor.

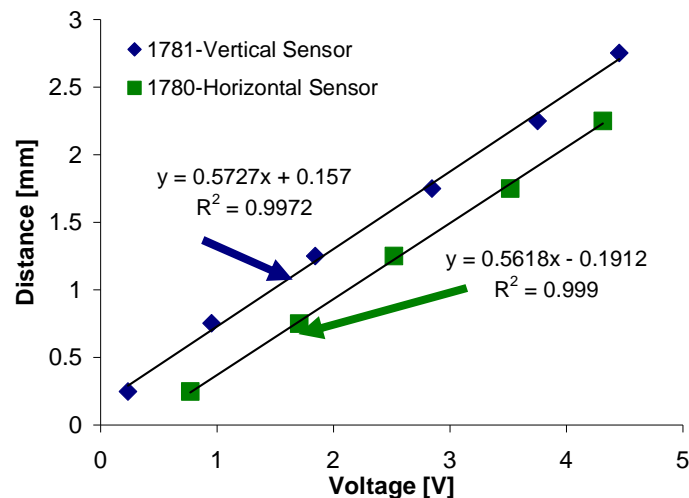


Figure D1: Distance versus output voltage for two optical sensors with calibration curves listed.

APPENDIX E

ROTOR WEAR DUE TO SEAL CONTACT

During testing with the brush seal and the hybrid brush seal (HBS), the imposed pressure difference causes the bristles to blow-down. Crudginton and Bowher [13] state the blow-down is caused by two separate actions: pressure driven compression of the bristles and aero-dynamic forces acting on the bristle tips.

Chapter VIII shows the (leakage) flow factor is lower in a HBS than in a conventional brush seal, even though both seals have nearly identical diametrical clearances, 0.52 mm, at room temperature and prior to pressurization. The reduction in flow factor (lesser leakage) is likely due to the HBS experiencing a greater degree of blow-down than the conventional brush seal.

The brush seal and HBS were tested with different discs. Both seals underwent ~20 hour of continuous testing with their respective disc. Post-test measurement of the disc OD surface roughness renders the magnitude and extent of contact between a test seal and its disc. Measurements of a disc OD show that no discernable change ($<0.0001''$). Figure E1 shows the surface roughness of the discs along the axial direction with the corresponding seal location noted on the test disc. The roughness reported is the average from measurements at three circumferential locations on the disc spaced 120° apart. The average circumferential variation in roughness is $\pm 0.04 \mu\text{m}$. Both discs show a significant reduction (polishing) in surface roughness at approximately 0.5'' where the seal is located. The disc for the tests with the HBS experiences a larger decrease in the surface roughness indicating a higher contact (larger blow-down). Note that in the HBS the disc is in contact with the seal resilient pads. On the other hand, with the brush seal, the contact is with the bristle tips.

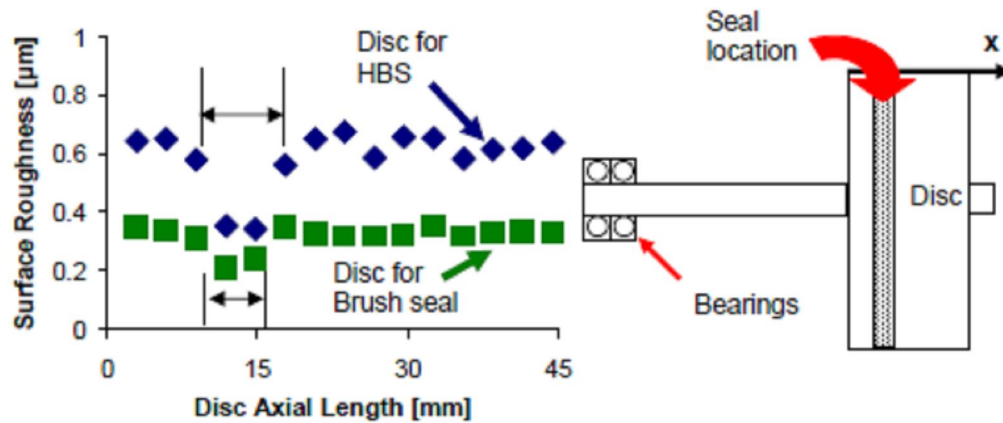


Figure E1: Surface roughness versus axial length of the test discs after ~20 hours of use with side view of shaft and disc. Disc for HBS and brush seal with OD of 165.48 mm and 166.81 mm, respectively.

Figure E2 displays the test disc for the HBS measurements after ~20 hours of operation. The axial wear mark is noticeable where the polishing occurs. Further, a change in the disc coloration is readily apparent due to the operation of the disc at high temperature.



Figure E2: Surface roughness versus axial length of the test discs after ~20 hours of use with side view of shaft and disc. Disc for HBS and brush seal with OD of 165.48 mm and 166.81 mm, respectively.

VITA

Name: Zachary Spencer Ashton

Address: Department of Mechanical Engineering, 3123 TAMU,
College Station, TX 77843, USA

Email: txashtons@gmail.com

Education: B.S., Mechanical Engineering, Clemson University,
Clemson, SC, 2007
M.S., Mechanical Engineering, Texas A&M University,
College Station, TX, 2009

Permanent Address: 6633 Canoga Ave
Canoga Park, CA, 91303, USA